

TECHNICAL UNIVERSITY OF CRETE
ELECTRICAL AND COMPUTER ENGINEERING DEPARTMENT
TELECOMMUNICATIONS DIVISION



Distributed (Network) Sequence Detection For Batteryless Internet Of Things (IoT)

by

Michail Ouroutzoglou

A THESIS SUBMITTED IN PARTIAL FULFILLMENT OF
THE REQUIREMENTS FOR THE DIPLOMA OF
ELECTRICAL AND COMPUTER ENGINEERING

July 2019

THESIS COMMITTEE

Professor Aggelos Bletsas, *Thesis Supervisor*

Professor George N. Karystinos

Associate Professor Vasilis Samoladas

Abstract

Batteryless Gen2 RFID and other Internet-Of-Things (IoT) tags communicate via means of reflection radio, i.e., backscattering. This is achieved by alternating the antenna of the tag between two different loads/states, one for RF energy reflection, and one for RF energy harvesting. Since the tag is passive, i.e., batteryless, it needs to ensure that 50% of the time, its antenna terminates in the harvesting state. This is possible with the use of line codes like Miller 2/4/8. However, line codes ensure powering in the case that the tag can be powered in the first place. Considering the low RF harvesting sensitivity of contemporary tags, the illuminating source needs to be very close (order of a few meters) to the tag in order to power it. The problem of bringing the illuminator closer to the tags has troubled the research community, inspiring the use of multiple expensive RF coaxial cables, amplifiers and multiplexers, or other monostatic front-ends wired to baseband processing units. This work provides a multistatic RFID interrogating solution, based on Ethernet-connected software defined radios (SDRs). However, this multistatic proposal raises important challenges, e.g., carrier frequency offset (CFO) and timing constraints, not highlighted in existing monostatic setups. Most importantly, with the introduction of CFO, coherent detection faces performance issues. This work addresses the above challenges and offers a robust, low-complexity and high-performance noncoherent sequence detection algorithm, that reliably detects the backscattered data. The proposed linear complexity Miller 2/4/8 sequence detection algorithm performs near-optimally (in terms of bit error rate), even compared to ideal coherent sequence detection. It is experimentally shown with commercial Gen2 RFID tags that the proposed architecture is able to both extend the reading range (reader-to-illuminator ≥ 30 m), as well as cover a large area with inexpensive

SDRs and Ethernet infrastructure (instead of expensive RF cables). Thus, a robust, low-cost, high-performance Ethernet-based multistatic RFID interrogation setup is offered that could potentially inspire the convergence of contemporary (e.g., LAN) or future (e.g., cellular) network infrastructure with the RFID industry.

Thesis Supervisor: Professor Aggelos Bletsas

Acknowledgements

First, I want to thank my supervisor Prof. Aggelos Bletsas for the guidance, lessons, trust, and support he offered me all the way from the 3rd year, up to my graduation. I wouldn't be the same person without him.

The whole team from the Bletsas Group, and especially, my colleague and close friend, Georgios Vougioukas, for the great times we had together carrying out experiments, him being available to offer advice for my problems, as well as being a great guy to hang out with.

My closest friends, Iasonas C., Christos P., Thodoris C. and Thanasis T., you guys are the best.

Finally, I want to give a special thanks to my family for believing in me, and supporting me and my decisions throughout my life. For that, I am ever grateful.

Table of Contents

Table of Contents	5
List of Figures	7
1 Introduction	10
1.1 Introduction	10
1.2 Notation	13
1.3 System Model	14
1.3.1 Signal Model	14
1.3.2 Monostatic Setup	15
2 Industrial Gen2 RFID Protocol & Miller Line Codes	17
2.1 Industrial Gen2 RFID Protocol	17
2.2 Miller Line Codes	18
2.2.1 Miller Based Signal Model	19
2.2.2 Zero-Centered Miller Coding	20
3 Miller Sequence Detection Algorithms	23
3.1 $\mathcal{O}(N)$ Complexity Optimal Coherent Sequence Detection	23
3.2 $\mathcal{O}(N)$ Complexity Noncoherent Sequence Detection	26
3.2.1 Algorithm	29
3.2.2 Algorithm Notation	30
4 Multistatic RFID Reader Architecture	32
4.1 Software Implementation with SDRs over Ethernet	32
4.2 Real Time CFO Estimation/Housekeeping Tasks	35
4.3 Limitations	39

5 Numerical Results	40
5.1 Simulation	40
5.2 Experimentation	43
5.2.1 Monostatic Setup	44
5.2.2 Multistatic Setup	46
6 Conclusion	50
6.1 Conclusion	50
6.2 Future Work	50
Bibliography	52

List of Figures

1.1	A closer look into an RFID/IoT tag. Observe how the tag terminates its antenna on two different loads/states, Z0 and Z1. Z0 is the “RF reflecting” state, and Z1 is the “RF absorbing” state.	11
1.2	Captured experimental RFID interrogation using apparatus of Fig. 5.3. The amplitude of the baseband samples is plotted.	14
2.1	An example of Miller 2/4/8 waveforms. The bit boundaries are defined by black vertical dashes.	18
2.2	Permitted symbol transitions according to Miller line coding.	20
3.1	Toy example of the proposed algorithm, on a partial trellis diagram. $W_{n,i}$ refers to the complex weight of the n -th bit to be $\hat{\mathbf{x}}_m[n] = \hat{\mathbf{S}}_{mi}$. $V_{n,i}$ refers the complex cumulative weight of the surviving path that the n -th bit at the i -th state propagates forward. Note that the absolute values of the cumulative weights are compared, but instead, the complex value of the winning path is propagated to the next bit.	28
4.1	Proposed multistatic architecture for real-time, Ethernet-based RFID tag interrogation. Multiple inexpensive SDRs are employed.	33

4.2	The vision of the proposed architecture. Multiple SDR transmitters/illuminators are deployed in a warehouse, and a single SDR receiver. Each illuminator activates a specific sector, due to the tag's RF harvesting sensitivity. Assuming multiple transmitters, a large area can be covered. The system avoids lossy and expensive coaxial extension cables and amplifier units by using conventional SDRs networked through Ethernet.	34
4.3	Distributed Gen2 RFID interrogation, captured from bistatic operation using 2 USRP N200 SDRs (one for Tx and one for Rx).	35
4.4	Block diagram that showcases the flow of the generated/received samples, through the various processing stages of the proposed system.	36
4.5	A simple schematic of a phase locked loop (PLL) used to track and compensate the CFO.	37
4.6	Simulated cumulative density function (CDF) of the absolute residual CFO after compensation using either a PLL or a heuristic method.	38
4.7	SDR-captured experimental waveforms (Top) & respective scatter plots (Bottom) of the received waveforms. Received waveform prior to CFO compensation (Left), after PLL-based CFO removal (Middle) and after DC compensation & synchronization (Right).	39
5.1	BER performance of the monostatic model with perfect CFO and DC compensation. The length of the sequence is $N = 128$ bits.	41

5.2	BER of the bistatic model with imperfect CFO compensation (using PLL) and dc offset correction. Performance gaps is demonstrated between coherent (with either perfect (Prf.Ch) or estimated channel (Est.)) and noncoherent detection, under Rayleigh and Rician fading conditions ($k_{CR} = k_{CT} = 20$). The case of perfect CFO and DC compensation is also given, as a baseline (All Prf.).	42
5.3	Monostatic setup used to extract experimental results for the proposed noncoherent detection algorithm.	44
5.4	Comparison of experimental BERs extracted on a monostatic RFID setup, using various detection algorithms.	45
5.5	Monostatic setup with commercial RFID reader under harsh indoor conditions. This offered a baseline for the tag reading distance. With 15 dBm Tx power, a maximum communication range of 1.1 m was achieved, while for 30 dBm the range increased to 4.5 m.	46
5.6	The proposed multistatic setup facilitating two USRPs as carrier sources/illuminators operating at 15 dBm alongside an RTL-SDR (or a USRP) as a receiver. The architecture offers increased coverage with multiple distributed SDR illuminators that function in a time-division manner and networked over Ethernet.	47
5.7	Demonstration of how a bistatic setup utilizing a single USRP as Tx (15 dBm) and a USRP or RTL-SDR as Rx, can increase reading range. Carrier-to-receiver ranges of at least 30 meters were observed, for a carrier-to-tag distance of 90 cm.	48
6.1	Would it be possible for contemporary (e.g., LAN) or future (e.g., cellular) network infrastructure to interrogate commercial Gen2 RFID or other IoT tags?	51

Chapter 1

Introduction

1.1 Introduction

Radio frequency identification (RFID) tags, as well as other internet of things (IoT) tags, communicate via means of reflection radio, i.e., backscattering. Backscattering means that part of the impinging signal, on the tag antenna, is reflected back to “air”. This is achieved by intentionally mismatching the antenna’s terminating load, so that part of the RF energy is absorbed, and the rest is backscattered. In this work, the tags of interest are mainly passive Gen2 RFID tags [1], however, this work can be applied as is to other IoT tags.

A Gen2 tag performs backscattering by terminating its antenna between two conflicting loads/states (Fig. 1.1). Load Z0 open-circuits the tag antenna, thus, the tag absorbs no energy and maximizes its reflection coefficient. However, in state Z1 there is “perfect” matching, which results in maximum power transfer, for RF energy harvesting, reducing the reflection coefficient to zero. Note that these states/load define two discrete energy/-line levels for the backscattered signal, one High and one Low (Z0 and Z1, respectively). However, these two levels do *not* represent bit-1 and bit-0. As already mentioned, Gen2 tags are passive, i.e., batteryless, and they harvest energy from the impinging signal (state Z1). Thus, in order to ensure the tag’s powering, no matter the backscattered bit sequence, line codes are introduced. The line codes used in Gen2 tags are FM0 and Miller 2/4/8.

Line codes, like the above, force the tags to switch between states Z0 and Z1 on a 50% duty cycle, ensuring energy harvesting, for every possible backscattered sequence. Additionally, line codes introduce memory in the backscattered signal, thus offering coding gain, which if taken into account,

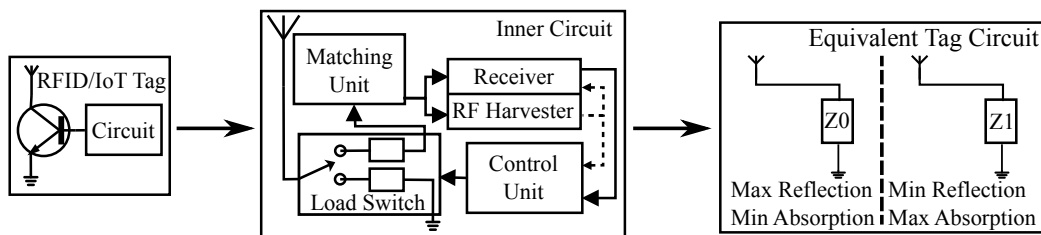


Figure 1.1: A closer look into an RFID/IoT tag. Observe how the tag terminates its antenna on two different loads/states, Z_0 and Z_1 . Z_0 is the “RF reflecting” state, and Z_1 is the “RF absorbing” state.

it can enhance the data detection. Finally, this memory enforces specific transitions between symbols (line coded bits), enabling the reader to discern between a noise signal (*ghost* tag) and a real tag response.

The Gen2 protocol [1], defines how the tags operate. Tag interrogation occurs in the duration of a slot, in a framed slotted Aloha protocol, as shown in Fig. 1.2. The tag interrogation will be thoroughly discussed down the road. However, it should be noted that there is a strict time limitation that the Gen2 protocol imposes on the reader, which if not met, times out the tags, ending the interrogation. This constraint creates all sorts of problems that will be discussed and solved later in this work.

Work in [2] offers precious insight on the topic of coherent sequence detection for FM0 and Miller line coding. The influential work of [3, 4] offers approximations to the maximum likelihood sequence detection (MLSD) under presence of unknown parameters (e.g., unknown channel). Research on generalized likelihood ratio test (GLRT)-optimal noncoherent sequence detection for FM0, with log-linear complexity (to the sequence length), is offered in [5]. The aforementioned log-linear algorithm, is experimentally tested on an SDR-based environment using industrial Gen2 RFID tags, in the work of [6]. [7] analyses an algorithm with log-linear complexity, that performs GLRT-optimal noncoherent MSK detection.

Research is conducted in [8], where an algorithm is offered that can perform noncoherent detection, with low complexity, perhaps linear to the sequence length. However, there is no proof that it will perform almost as good as coherent detection, nor that it will still operate in an unideal environment

containing carrier frequency and DC offset. According to the authors of [8], the bit error rate performance can be enhanced, but at the expense of increasing the complexity, e.g., from linear to quadratic.

Findings on bistatic [9–14] and multistatic [15] backscatter radio demonstrate that the telecommunication range can be substantially increased by such architectures. Additionally, diversity gain and higher link budget can be achieved through exploitation of the dyadic [16], non-linear nature of wireless propagation. Clearly, a multistatic architecture greatly outperforms a monostatic setup, but this comes at the cost of increased installation cost and complexity.

Both industry and individual groups, have proposed several approaches on how to bring the Tx antenna in the vicinity of the tag, in order to combat its limited RF harvesting capabilities. Most notable is the work of [17] where networks of multiplexers, high-quality amplifier and coaxial cables are used in an effort to spread more illuminators in a large area. However, this approach is quite expensive. Further work is offered in [18], proposing that multiple monostatic devices are wired to a baseband processing unit.

On the general spectrum of bistatic backscatter radio, there are tags capable of backscattering signals in a specific protocol format, such as WiFi [19], Lora [20] as well as BLE [14, 21].

The purpose of this work is to offer a novel linear complexity (to the sequence length) noncoherent Miller 2/4/8 sequence detection algorithm, in addition to providing extensive results both in a simulated environment *and* in a real-world experimental testbed. The simulated results are extracted under Rice and Rayleigh fading, while there is a plethora of results (simulated and experimental), for both monostatic and bi/multistatic scenarios. Surprisingly, the proposed linear algorithm performs almost as good as perfect coherent sequence detection, even under the presence of residual carrier frequency and DC offset.

Additional research is offered in this work, specifically for the design of a multistatic RFID interrogation architecture, using Ethernet-based software defined radios (SDRs). The proposed multistatic setup can achieve reading distances of at least 30 m (reader-to-illuminator), whereas monostatic setups

are limited to a few meters (1.1 m for 15 dBm Tx power). Furthermore, SDRs are becoming less expensive, and the cost of the infrastructure is really low, considering that the Ethernet is omnipresent. Instead, RF cables, amplifiers, and proprietary devices are expensive.

It turns out that the two components of this work, can be combined to provide a low-cost, low-complexity and high-performance multistatic RFID interrogation system, thanks to smart signal processing, and inexpensive SDRs.

Chapter 2 describes the industrial Gen2 protocol, Miller line coding, and offers an important theorem; Chapter 3 describes the coherent and proposed noncoherent sequence detection algorithms; Chapter 4 analyses the SDR- & Ethernet-based multistatic setup of this work; Chapter 5 offers and studies simulated and experimental results. Chapter 6 concludes this work.

1.2 Notation

Notation: $\mathcal{CN}(\mathbf{m}, \mathbf{C})$ refers to the proper complex Gaussian distribution with mean vector \mathbf{m} and covariance matrix \mathbf{C} . w^H denotes the conjugate of a complex scalar w ; in the case of a complex vector \mathbf{v} , conjugate transpose (Hermitian) is denoted also as \mathbf{v}^H . The inner product of two complex vectors $\mathbf{v}_1, \mathbf{v}_2$ is denoted as $\langle \mathbf{v}_1, \mathbf{v}_2 \rangle = \mathbf{v}_1^H \mathbf{v}_2$. $\Re\{w\}$ and $\Im\{w\}$ yield the real and imaginary part of complex scalar w , respectively. The Euclidean norm of complex vector \mathbf{x} is denoted as $\|\mathbf{x}\|_2 = \sqrt{\mathbf{x}^H \mathbf{x}}$. $\mathbb{I}(\cdot)$ is an indicator function that returns 1 if its argument is true and 0, otherwise. Finally, $\mathcal{U}(a, b)$ refers to the uniform probability distribution in the range $[a, b]$.

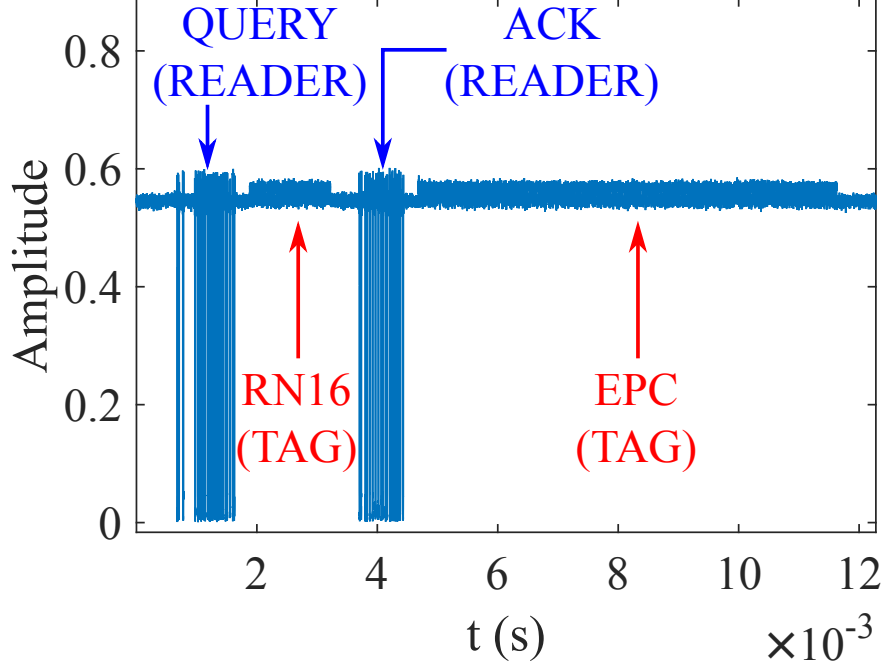


Figure 1.2: Captured experimental RFID interrogation using apparatus of Fig. 5.3. The amplitude of the baseband samples is plotted.

1.3 System Model

1.3.1 Signal Model

According to prior art [12], the received samples (from the Rx SDR) adhere to the following signal model:

$$\begin{aligned}
 y[k] &= \left(\sqrt{2P_c} h_{\text{CR}} + \sqrt{2P_c} h_{\text{S}} x_{\text{tag}}[k] \right) e^{-j(2\pi\Delta f k T_s + \Delta\phi_{\text{R}})} + n[k] \\
 &= (m_{\text{dc}} + m_{\text{tag}} x_{\text{tag}}[k]) e^{-j(2\pi\Delta f k T_s + \Delta\phi_{\text{R}})} + n[k].
 \end{aligned} \tag{1.1}$$

Notation-wise, the sampling period of the Rx SDR is denoted as T_s , the carrier frequency and phase offset (CFO & CPO) are denoted as Δf and $\Delta\phi_{\text{R}}$, respectively. The tag backscattered signal is denoted as $x_{\text{tag}}[k] \in \{\Gamma_0, \Gamma_1\}$, with Γ_0, Γ_1 referring to the reflection coefficients of the tag (these correspond to the two backscattering states, i.e., energy reflection and absorption). Note

that these states correspond to low and high energy states, however, they are not equivalent to logical bits “0” & “1”. The Tx power is denoted P_c ; tag scattering efficiency is denoted as $s \in (0, 1)$; thermal noise of the Rx SDR is denoted as $n[k] \sim \mathcal{CN}(0, \sigma_n^2)$, with $\sigma_n^2 = N_0 W_{rx}$, N_0 referring to the noise power spectral density and W_{rx} corresponding to the bandwidth of the receiving SDR. Obviously, noise samples with different timestamps are independent. Flat fading is assumed throughout the tag interrogation, and the effects of multiple paths are modeled by $h_{CR} \in \mathbb{C}$ and $h = h_{CT}h_{TR} \in \mathbb{C}$:

$$h_q \sim \mathcal{CN}\left(\sqrt{\frac{k_q}{k_q + 1}} \sigma_q, \frac{\sigma_q^2}{k_q + 1}\right), \quad q \in \{\text{CR}, \text{CT}, \text{TR}\}, \quad (1.2)$$

where CR refers to the carrier-to-receiver link, CT refers to the carrier-to-tag link, TR refers to the tag-to-receiver link, and $\sigma_q^2 = \mathbb{E}[|h_q|^2]$. The power ratio of the direct (Line of Sight) link and over the scattered paths is modeled by the parameter k_q . For $k_q > 0$ Rician fading is obtained, whereas for $k_q = 0$ it turns into Rayleigh fading.

1.3.2 Monostatic Setup

The signal model of Eq. (1.1) can be further simplified under the assumption of a monostatic setup. In this case, a single device performs both transmission and reception, utilizing the same oscillator for both operations; thus, $\Delta f = \Delta\phi_R = 0$. The complex gain parameter h_{CR} now refers to the leakage between transmit and receive chain. Due to the proximity of the antenna and the tag, reciprocity is assumed [15], i.e., $h_{CT} = h_{TR}$, thus, $h = h_{CT}^2$. Furthermore, the structural mode parameter of the tag, $A_s \in \mathbb{C}$, is absorbed in the DC term m_{dc} .

Under the assumption of matched filtering, perfect DC offset removal and synchronization, the signal model of Eq. (1.1) can be rewritten as [22]:

$$y[i] = \tilde{h} x_{\text{tag}}[i] + w[i], \quad (1.3)$$

where $\tilde{h} = L\sqrt{2P_c}h$ and L is the oversampling factor. Specifically, bit duration is denoted as T_b and considering that each “low” or “high” energy/line level of the baseband signal is a part of the bit, i.e., a *chip*, then $L = \frac{T_b}{2mT_s}$ is the number of samples per chip; integer $m \in \{2, 4, 8\}$ refers to the Miller m line code in use. For each chip index i , it holds that $x_{\text{tag}}[i] \in \{0, 1\}$ and $w[i] \sim \mathcal{CN}(0, L\sigma_n^2)$. The signal model of Eq. (1.3) is valid for both monostatic, as well as bistatic setups; however, in the latter case, perfect CFO, CPO and DC compensation is assumed. In the simulation, but also in experimental results for the bistatic (or multistatic case), such ideal assumptions are dropped; instead realistic compensation methods are used, that are bound to leave undesired residual components in our samples.

Chapter 2

Industrial Gen2 RFID Protocol & Miller Line Codes

2.1 Industrial Gen2 RFID Protocol

According to the Gen2 protocol, available in [1], the RFID tags are interrogated during a slot of a framed slotted Aloha (FSA) protocol. SDR-captured signal of an interrogation is available in Fig. 1.2, with the various parts of the process highlighted. The interrogation process starts with the reader transmitting a continuous wave (CW),¹ that activates the tags (through RF energy harvesting) in the vicinity of the illuminator. Shortly after, the reader transmits a QUERY command, which initializes various tag parameters, e.g., tag rate, line code, and FSA slots. Assuming a single tag, and a single FSA slot (for simplicity purposes), the tag will generate and backscatter a random 16-bit sequence named RN16. The Reader has to receive this backscattered sequence, detect it, and transmit an appropriate acknowledgement (ACK) message back to the tag, according to the RN16 bits. The tag compares the ACK and the RN16 bits; if they match, the handshake is successful, and thus, the tag backscatters its 128-bit payload, which includes the electronic product code (EPC) 96-bit identification information. It needs to be mentioned that each time the tag backscatters a message, it precedes it with a known preamble sequence. There is also the option to activate an additional pilot (known) sequence, that can be explicitly used for channel estimation and coherent detection, however activating it will decrease the tag reading rate.

¹The CW is transmitted at all times except during Reader commands, e.g., QUERY, ACK.

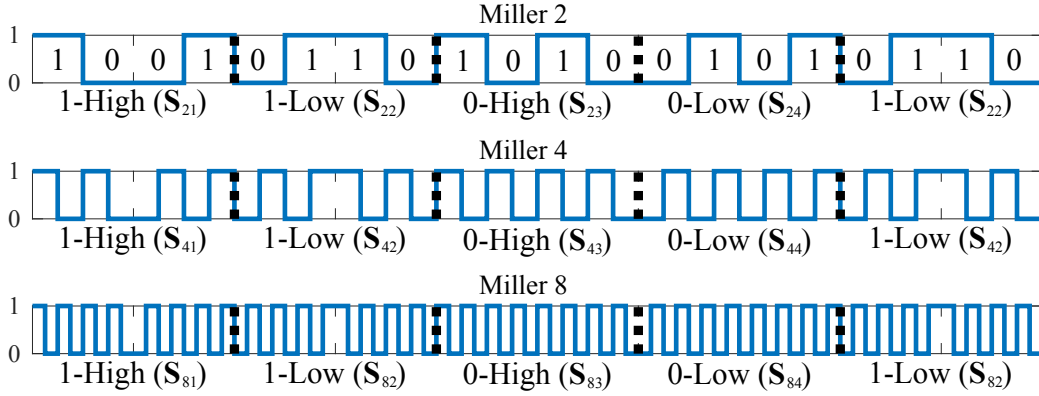


Figure 2.1: An example of Miller 2/4/8 waveforms. The bit boundaries are defined by black vertical dashes.

2.2 Miller Line Codes

In Miller line codes, each logical bit is coded by two possible symbols/waveforms (4 in total). Generally, the line level of Miller 2/4/8 waveforms transitions continuously throughout the duration. However, bit-1 waveforms (S_{m1} , S_{m2}) have constant level at the middle of the bit, whereas, bit-0 waveforms (S_{m3} , S_{m4}) adhere to the above rule. As far as symbol transitions are concerned, the line level at the start of each symbol must be different than that of the preceding symbol (i.e., High \rightarrow Low & Low \rightarrow High). A transition from Bit-0 to Bit-1 is the exception to that rule, in which case the line level must be the same to at the start of both symbols

The way each Miller line code encodes its symbols is shown in Fig. 2.1. The allowed transitions, depicted in Fig. 2.2, between Miller m symbols are fixed independently of the $m \in \{2, 4, 8\}$. As far as notation is concerned, 1-High and 1-Low are the two symbols/waveforms encoding the logical bit “1”, whereas 0-High and 0-Low refers to bit “0”, respectively. Note that the keywords “High” and “Low” refer to the line level at the start of the symbol/waveform. For Miller m , these four symbols are expressed as $S_m = \{S_{m1}, S_{m2}, S_{m3}, S_{m4}\}$. According to Miller line coding, specific transitions are allowed, for example, if the last transmitted symbol is 1-High (S_{m1}) then the next allowed symbols are either 1-Low (S_{m2}) or 0-Low (S_{m4}),

for bit-1 and bit-0, respectively. Also, note (see last transition in Fig. 2.1) that when there is transition from bit-0 to bit-1, the line level remains the same, i.e., 0-Low \rightarrow 1-Low. Miller 4 (8) differs from Miller 2 in the sense that the symbols have $2\times$ ($4\times$) more chips per bit (Fig. 2.1). In addition to that, solely changing the line code of Gen2 RFID tags, from Miller 2 to 4 (8), yields a $2\times$ ($4\times$) longer bit duration, due to unchanged (constant) chip duration.

2.2.1 Miller Based Signal Model

Under the assumption of Miller m , $m \in \{2, 4, 8\}$, line coding as well as N backscattered bits, Eq. (1.3) is expressed as:

$$\mathbf{y}_m[n] = \begin{bmatrix} y[4n+0] \\ y[4n+1] \\ \vdots \\ y[4n+2m-1] \end{bmatrix} = \tilde{h}\mathbf{x}_m[n] + \mathbf{w}_m[n], \quad n = 0, 1, \dots, N-1, \quad (2.1)$$

where $\{\mathbf{w}_m[n]\}$ are i.i.d., $\mathbf{w}_m[n] \sim \mathcal{CN}(\mathbf{0}, L\sigma_n^2\mathbf{I}_{2m})$, and backscattered symbol vectors $\mathbf{x}_m[n] \in \mathbb{S}_m = \{\mathbf{S}_{m1}, \mathbf{S}_{m2}, \mathbf{S}_{m3}, \mathbf{S}_{m4}\}$, with symbols in set \mathbb{S}_m defined as:

- Miller 2

$$\begin{aligned} \mathbf{S}_{21} &= \begin{bmatrix} 1 & 0 & 0 & 1 \end{bmatrix}^T, \quad \mathbf{S}_{22} = \begin{bmatrix} 0 & 1 & 1 & 0 \end{bmatrix}^T, \\ \mathbf{S}_{23} &= \begin{bmatrix} 1 & 0 & 1 & 0 \end{bmatrix}^T, \quad \mathbf{S}_{24} = \begin{bmatrix} 0 & 1 & 0 & 1 \end{bmatrix}^T, \end{aligned}$$

- Miller 4

$$\begin{aligned} \mathbf{S}_{41} &= \begin{bmatrix} \mathbf{S}_{23}^T & \mathbf{S}_{24}^T \end{bmatrix}^T, \quad \mathbf{S}_{42} = \begin{bmatrix} \mathbf{S}_{24}^T & \mathbf{S}_{23}^T \end{bmatrix}^T, \\ \mathbf{S}_{43} &= \begin{bmatrix} \mathbf{S}_{23}^T & \mathbf{S}_{23}^T \end{bmatrix}^T, \quad \mathbf{S}_{44} = \begin{bmatrix} \mathbf{S}_{24}^T & \mathbf{S}_{24}^T \end{bmatrix}^T, \end{aligned}$$

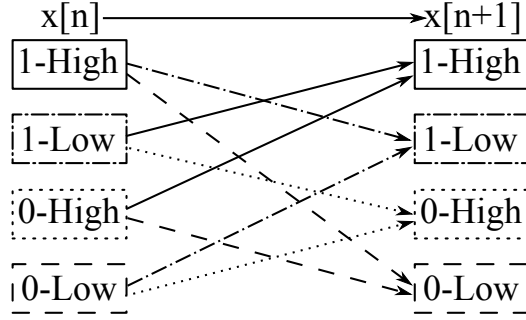


Figure 2.2: Permitted symbol transitions according to Miller line coding.

- Miller 8

$$\mathbf{S}_{81} = \begin{bmatrix} \mathbf{S}_{23}^T & \mathbf{S}_{23}^T & \mathbf{S}_{24}^T & \mathbf{S}_{24}^T \end{bmatrix}^T, \quad \mathbf{S}_{82} = \begin{bmatrix} \mathbf{S}_{24}^T & \mathbf{S}_{24}^T & \mathbf{S}_{23}^T & \mathbf{S}_{23}^T \end{bmatrix}^T,$$

$$\mathbf{S}_{83} = \begin{bmatrix} \mathbf{S}_{23}^T & \mathbf{S}_{23}^T & \mathbf{S}_{23}^T & \mathbf{S}_{23}^T \end{bmatrix}^T, \quad \mathbf{S}_{84} = \begin{bmatrix} \mathbf{S}_{24}^T & \mathbf{S}_{24}^T & \mathbf{S}_{24}^T & \mathbf{S}_{24}^T \end{bmatrix}^T.$$

2.2.2 Zero-Centered Miller Coding

It can be easily observed in Fig. 2.1, that backscatter Miller m symbols are centered around $\beta = \frac{1}{2}$. Thus, this β constant can be subtracted from each element of the symbol vector and result in a zero-centered Miller line code. This can also be seen through the following operations:

$$\begin{aligned} \mathbf{S}_{mi} &= \mathbf{S}_{mi} + (\beta - \beta)\mathbf{1}_{2m} = (\mathbf{S}_{mi} - \beta\mathbf{1}_{2m}) + \beta\mathbf{1}_{2m} = \hat{\mathbf{S}}_{mi} + \beta\mathbf{1}_{2m} \Rightarrow \\ \hat{\mathbf{S}}_{mi} &= \mathbf{S}_{mi} - \beta\mathbf{1}_{2m}, \quad \forall m \in \{2, 4, 8\}, \quad \forall i \in \{1, 2, 3, 4\}. \end{aligned} \quad (2.2)$$

Notation-wise, $\mathbf{1}_{2m}$ is a $2m \times 1$ vector of “1”s, $\hat{\mathbf{S}}_m = \{\hat{\mathbf{S}}_{m1}, \hat{\mathbf{S}}_{m2}, \hat{\mathbf{S}}_{m3}, \hat{\mathbf{S}}_{m4}\}$ is the set of zero-centered Miller m symbols. Below the zero-centered symbols for Miller 2 are offered as an example:

$$\begin{aligned} \hat{\mathbf{S}}_{21} &= \frac{1}{2} \begin{bmatrix} +1 & -1 & -1 & +1 \end{bmatrix}^T, \quad \hat{\mathbf{S}}_{22} = -\hat{\mathbf{S}}_{21}, \\ \hat{\mathbf{S}}_{23} &= \frac{1}{2} \begin{bmatrix} +1 & -1 & +1 & -1 \end{bmatrix}^T, \quad \hat{\mathbf{S}}_{24} = -\hat{\mathbf{S}}_{23}. \end{aligned}$$

The rest symbols for Miller 4/8 are defined accordingly.

Under the hypothesis of perfect channel \tilde{h} knowledge,² and Miller m line code, an equivalent zero-centered signal model can be derived based on Eq. (2.1) as follows:

$$\begin{aligned}\hat{\mathbf{y}}_m[n] &\triangleq \mathbf{y}_m[n] - \beta\tilde{h}\mathbf{1}_{2m} \\ &= \tilde{h}(\mathbf{x}_m[n] - \beta\mathbf{1}_{2m}) + \mathbf{w}_m[n] \\ &\stackrel{(2.2)}{=} \tilde{h}\hat{\mathbf{x}}_m[n] + \mathbf{w}_m[n], \quad n = 0, 1, \dots, N-1,\end{aligned}\quad (2.3)$$

where system parameter β is user-defined and thus known a priori; data vectors $\hat{\mathbf{x}}_m$ are zero-centered Miller m symbols, thus $\hat{\mathbf{x}}_m \in \hat{\mathcal{S}}_m$.

Taking advantage of the structure of Miller symbols, the following can be shown for every Miller m symbol:

$$\begin{aligned}\langle \hat{\mathbf{S}}_{mj}, \mathbf{S}_{mi} \rangle &= \langle \hat{\mathbf{S}}_{mj}, \hat{\mathbf{S}}_{mi} + \beta\mathbf{1}_{2m} \rangle \\ &= \langle \hat{\mathbf{S}}_{mj}, \hat{\mathbf{S}}_{mi} \rangle + \beta \langle \hat{\mathbf{S}}_{mj}, \mathbf{1}_{2m} \rangle \\ &= \langle \hat{\mathbf{S}}_{mj}, \hat{\mathbf{S}}_{mi} \rangle.\end{aligned}\quad (2.4)$$

The above holds due to the fact that $\langle \hat{\mathbf{S}}_{mj}, \mathbf{1}_{2m} \rangle = 0$, as a result of the equal number of $\{+\frac{1}{2}, -\frac{1}{2}\}$ elements in each vector $\hat{\mathbf{S}}_{mj}$.

All the above helpful equations boil down to the following derivation:

$$\begin{aligned}\langle \hat{\mathbf{S}}_{mj}, \hat{\mathbf{y}}_m[n] \rangle &= \langle \hat{\mathbf{S}}_{mj}, \tilde{h}\hat{\mathbf{x}}_m[n] + \mathbf{w}_m[n] \rangle \\ &= \tilde{h} \langle \hat{\mathbf{S}}_{mj}, \hat{\mathbf{x}}_m[n] \rangle + \langle \hat{\mathbf{S}}_{mj}, \mathbf{w}_m[n] \rangle \\ &\stackrel{(2.4)}{=} \tilde{h} \langle \hat{\mathbf{S}}_{mj}, \mathbf{x}_m[n] \rangle + \langle \hat{\mathbf{S}}_{mj}, \mathbf{w}_m[n] \rangle \\ &= \langle \hat{\mathbf{S}}_{mj}, \tilde{h}\mathbf{x}_m[n] + \mathbf{w}_m[n] \rangle \\ &= \langle \hat{\mathbf{S}}_{mj}, \mathbf{y}_m[n] \rangle.\end{aligned}\quad (2.5)$$

This finding is formally stated below:

²This hypothesis is not required, but this is proved later in this work.

Theorem 1. *Let $\hat{\mathbf{x}}_m[n] \in \hat{\mathcal{S}}_m$, $m \in \{2, 4, 8\}$, $\mathbf{y}_m[n]$ any β -centered Miller m signal model and $\hat{\mathbf{y}}_m[n]$ its equivalent zero-centered signal model. The following holds:*

$$\langle \hat{\mathbf{x}}_m[n], \hat{\mathbf{y}}_m[n] \rangle = \langle \hat{\mathbf{x}}_m[n], \mathbf{y}_m[n] \rangle. \quad (2.6)$$

This theorem indicates that the residual DC term in the signal model (after imperfect compensation), does not contribute in the inner products of Eq. (2.6). Building upon the previous statement, centering of the backscattered waveform is not required. This means that estimation/knowledge of channel \tilde{h} is not needed, thus the initial assumption of perfect channel knowledge can be dropped.

The importance of this theorem stems from the fact that inner products in the form of Eq. (2.6), appear in the metrics of the coherent and proposed noncoherent sequence detection schemes of Chap. 3. This allows the noncoherent algorithm to be truly noncoherent.

Chapter 3

Miller Sequence Detection Algorithms

3.1 $\mathcal{O}(N)$ Complexity Optimal Coherent Sequence Detection

Coherent Miller sequence detection has already been explored in prior art [2, 23], however, in this work it will be looked under a different angle, in terms of derivation, as well as extending the algorithm to all β -centered signal models, by using Th.1.

The primary reason that the coherent sequence detection is discussed is because it provides a benchmark for the performance of this work's linear noncoherent sequence detection algorithm.

Miller line code introduces memory on the tag backscattered symbol sequence. Thus, according to Fig. 2.1 and Fig. 2.2, there are rules that dictate which transitions are allowed. As a result, consecutive symbols are correlated, and thus, sequence detection is necessary in order to take into account the induced memory. Note that the underlying bits are independent, but not the encoded symbols.

Coherent sequence detection is derived by maximizing joint conditional probability density function (PDF) of the whole sequence. The conditional PDF is defined given knowledge of the channel parameter \tilde{h} , and thus, the signal model of Eq. (2.3) can replace the one defined in Eq. (2.1). The

conditional PDF $f(\cdot|\cdot)$ for a single bit is defined as:

$$f\left(\hat{\mathbf{y}}_m[n] \middle| \hat{\mathbf{x}}_m[n], \tilde{h}\right) \sim \mathcal{CN}(\tilde{h}\hat{\mathbf{x}}_m[n], L\sigma_n^2\mathbf{I}_{2m}) \quad (3.1)$$

$$\propto \exp\left(-\frac{1}{L\sigma_n^2} \left\| \hat{\mathbf{y}}_m[n] - \tilde{h}\hat{\mathbf{x}}_m[n] \right\|_2^2\right), \quad (3.2)$$

so the joint conditional PDF of the whole miller coded sequence is defined as:

$$f\left(\hat{\mathbf{y}}_m \middle| \hat{\mathbf{x}}_m, \tilde{h}\right) = \prod_{n=0}^{N-1} f\left(\hat{\mathbf{y}}_m[n] \middle| \hat{\mathbf{x}}_m[n], \tilde{h}\right), \quad (3.3)$$

with $\hat{\mathbf{y}}_m$, $\hat{\mathbf{x}}_m$ defined as the sets that contain all the $\hat{\mathbf{y}}_m[n]$, $\hat{\mathbf{x}}_m[n]$ symbols, respectively. It needs to be noted that the symbols $\hat{\mathbf{x}}_m[n]$ are not independent, and thus not all sequences are valid. Instead, it holds that $\hat{\mathbf{x}}_m \in \mathcal{X}_m$, where \mathcal{X}_m is a set containing all allowed (valid) N -bit Miller m coded sequences. Finally, the optimal sequence can be detected by solving a maximum likelihood (ML) problem:

$$\begin{aligned} \hat{\mathbf{x}}_m^{\text{ML}} &= \underset{\hat{\mathbf{x}}_m \in \mathcal{X}_m}{\operatorname{argmax}} \prod_{n=0}^{N-1} f\left(\hat{\mathbf{y}}_m[n] \middle| \hat{\mathbf{x}}_m[n], \tilde{h}\right) \\ &= \underset{\hat{\mathbf{x}}_m \in \mathcal{X}_m}{\operatorname{argmax}} \prod_{n=0}^{N-1} \exp\left(-\frac{1}{L\sigma_n^2} \left\| \hat{\mathbf{y}}_m[n] - \tilde{h}\hat{\mathbf{x}}_m[n] \right\|_2^2\right) \\ &= \underset{\hat{\mathbf{x}}_m \in \mathcal{X}_m}{\operatorname{argmin}} \sum_{n=0}^{N-1} \left\| \hat{\mathbf{y}}_m[n] - \tilde{h}\hat{\mathbf{x}}_m[n] \right\|_2^2 \\ &= \underset{\hat{\mathbf{x}}_m \in \mathcal{X}_m}{\operatorname{argmin}} \sum_{n=0}^{N-1} \left(\left\| \hat{\mathbf{y}}_m[n] \right\|_2^2 + \left\| \tilde{h}\hat{\mathbf{x}}_m[n] \right\|_2^2 - 2\Re \left\{ \left\langle \tilde{h}\hat{\mathbf{x}}_m[n], \hat{\mathbf{y}}_m[n] \right\rangle \right\} \right) \\ &\stackrel{(a)}{=} \underset{\hat{\mathbf{x}}_m \in \mathcal{X}_m}{\operatorname{argmax}} \sum_{n=0}^{N-1} \Re \left\{ \tilde{h}^H \langle \hat{\mathbf{x}}_m[n], \hat{\mathbf{y}}_m[n] \rangle \right\} \\ &\stackrel{\text{Th. 1}}{=} \underset{\hat{\mathbf{x}}_m \in \mathcal{X}_m}{\operatorname{argmax}} \sum_{n=0}^{N-1} \Re \left\{ \tilde{h}^H \langle \hat{\mathbf{x}}_m[n], \mathbf{y}_m[n] \rangle \right\}, \end{aligned} \quad (3.4)$$

where in (a) the fact that $\|\hat{\mathbf{x}}_m[n]\|_2^2 = \text{constant}, \forall \hat{\mathbf{x}}_m[n] \in \hat{\mathcal{S}}_m, \forall$ Miller m line code, was used.

The solution to the above ML problem can be found by use of the Viterbi algorithm (VA), which has linear (to the sequence length) complexity, on top of a trellis diagram, defined by allowed transitions shown in Fig. 2.2. Each node of the trellis has a weight defined as $W_{n,i} = \Re \left\{ \tilde{h}^H \langle \hat{\mathbf{x}}_m[n], \mathbf{y}_m[n] \rangle \right\}$, where n refers to the n -th bit of the sequence, and i refers to the state of the trellis diagram, in other words, $\hat{\mathbf{x}}_m[n] = \hat{\mathbf{S}}_{mi}$.

It is noted that coherent detection, assumes knowledge of the channel parameter \tilde{h} , however, in a realistic scenario it is not available, and thus, it needs to be estimated. In this work it is estimated using a least squares estimator on the known Gen2 preamble bits. Extra pilot bits can be activated to augment the channel estimation, however this will deteriorate the tag reading rate.

In Eq. (3.4) the use of Th. 1 allows the detector to jump from the zero-centered signal model of Eq. (2.3) back to the β -centered signal model of Eq. (2.1).

3.2 $\mathcal{O}(N)$ Complexity Noncoherent Sequence Detection

In this section, the novel, linear complexity, noncoherent Miller sequence detection algorithm will be discussed. Since the algorithm is noncoherent, the analysis will proceed considering the channel parameter \tilde{h} an unknown constant. Thus, the generalized likelihood ratio test (GLRT) sequence detection rule is derived. Although, this GLRT rule is not used to solve the sequence detection problem, it will be used as a guide for the derivation of proposed linear noncoherent sequence detection algorithm.

The derivation of the GLRT rule starts by finding the parameter \hat{h} that maximizes the aforementioned joint likelihood function:

$$\begin{aligned}
\hat{h} &= \operatorname{argmax}_{\tilde{h} \in \mathbb{C}} f(\hat{\mathbf{y}}_m | \hat{\mathbf{x}}_m, \tilde{h}) \\
&= \operatorname{argmin}_{\tilde{h} \in \mathbb{C}} \sum_{j=0}^{N-1} \left\| \hat{\mathbf{y}}_m[j] - \tilde{h} \hat{\mathbf{x}}_m[j] \right\|_2^2 \\
&= \operatorname{argmin}_{\tilde{h} \in \mathbb{C}} \sum_{j=0}^{N-1} \left(\|\hat{\mathbf{y}}_m[j]\|_2^2 + \tilde{h}^H \tilde{h} \|\hat{\mathbf{x}}_m[j]\|_2^2 \right. \\
&\quad \left. - \tilde{h}^H \langle \hat{\mathbf{x}}_m[j], \hat{\mathbf{y}}_m[j] \rangle - \tilde{h} \langle \hat{\mathbf{y}}_m[j], \hat{\mathbf{x}}_m[j] \rangle \right) \\
&= \operatorname{argmin}_{\tilde{h} \in \mathbb{C}} G(\tilde{h}, \hat{\mathbf{x}}_m, \hat{\mathbf{y}}_m). \tag{3.5}
\end{aligned}$$

Function $G(\tilde{h}, \hat{\mathbf{x}}_m, \hat{\mathbf{y}}_m)$ is minimized when:

$$\begin{aligned} \left. \frac{\partial}{\partial \tilde{h}} G(\tilde{h}, \hat{\mathbf{x}}_m, \hat{\mathbf{y}}_m) \right|_{\tilde{h}=\hat{h}} &= 0 \Leftrightarrow \\ \sum_{j=0}^{N-1} \hat{h}^H \|\hat{\mathbf{x}}_m[j]\|_2^2 &= \sum_{j=0}^{N-1} \langle \hat{\mathbf{y}}_m[j], \hat{\mathbf{x}}_m[j] \rangle \Leftrightarrow \\ \hat{h} &= \frac{\sum_{j=0}^{N-1} \langle \hat{\mathbf{x}}_m[j], \hat{\mathbf{y}}_m[j] \rangle}{\sum_{j=0}^{N-1} \|\hat{\mathbf{x}}_m[j]\|_2^2}. \end{aligned} \quad (3.6)$$

This channel estimate \hat{h} can now be plugged in the conditional PDF of Eq. (3.3), and through maximization the GLRT-optimal sequence can be extracted as follows:

$$\begin{aligned} \hat{\mathbf{x}}_m^{\text{GLRT}} &= \underset{\hat{\mathbf{x}}_m \in \mathcal{X}_m}{\operatorname{argmax}} \prod_{n=0}^{N-1} f(\hat{\mathbf{y}}_m[n] | \hat{\mathbf{x}}_m[n], \hat{h}) \\ &= \underset{\hat{\mathbf{x}}_m \in \mathcal{X}_m}{\operatorname{argmin}} \sum_{n=0}^{N-1} \left\| \hat{\mathbf{y}}_m[n] - \hat{h} \hat{\mathbf{x}}_m[n] \right\|_2^2 \\ &= \underset{\hat{\mathbf{x}}_m \in \mathcal{X}_m}{\operatorname{argmin}} \sum_{n=0}^{N-1} \left(\left\| \hat{h} \hat{\mathbf{x}}_m[n] \right\|_2^2 - 2 \Re \left\{ \hat{h}^H \langle \hat{\mathbf{x}}_m[n], \hat{\mathbf{y}}_m[n] \rangle \right\} \right) \\ &= \underset{\hat{\mathbf{x}}_m \in \mathcal{X}_m}{\operatorname{argmin}} \left(\left\| \hat{h} \right\|_2^2 \sum_{n=0}^{N-1} \|\hat{\mathbf{x}}_m[n]\|_2^2 - 2 \sum_{n=0}^{N-1} \Re \left\{ \hat{h}^H \langle \hat{\mathbf{x}}_m[n], \hat{\mathbf{y}}_m[n] \rangle \right\} \right) \\ &= \underset{\hat{\mathbf{x}}_m \in \mathcal{X}_m}{\operatorname{argmin}} \left(\frac{\left\| \sum_{j=0}^{N-1} \langle \hat{\mathbf{x}}_m[j], \hat{\mathbf{y}}_m[j] \rangle \right\|_2^2}{\sum_{j=0}^{N-1} \|\hat{\mathbf{x}}_m[j]\|_2^2} - 2 \frac{\left\| \sum_{j=0}^{N-1} \langle \hat{\mathbf{x}}_m[j], \hat{\mathbf{y}}_m[j] \rangle \right\|_2^2}{\sum_{j=0}^{N-1} \|\hat{\mathbf{x}}_m[j]\|_2^2} \right) \\ &= \underset{\hat{\mathbf{x}}_m \in \mathcal{X}_m}{\operatorname{argmax}} \left\| \sum_{n=0}^{N-1} \langle \hat{\mathbf{x}}_m[n], \hat{\mathbf{y}}_m[n] \rangle \right\|_2^2 \\ &\stackrel{\text{Th. 1}}{=} \underset{\hat{\mathbf{x}}_m \in \mathcal{X}_m}{\operatorname{argmax}} \left\| \sum_{n=0}^{N-1} \langle \hat{\mathbf{x}}_m[n], \mathbf{y}_m[n] \rangle \right\|_2^2. \end{aligned} \quad (3.7)$$

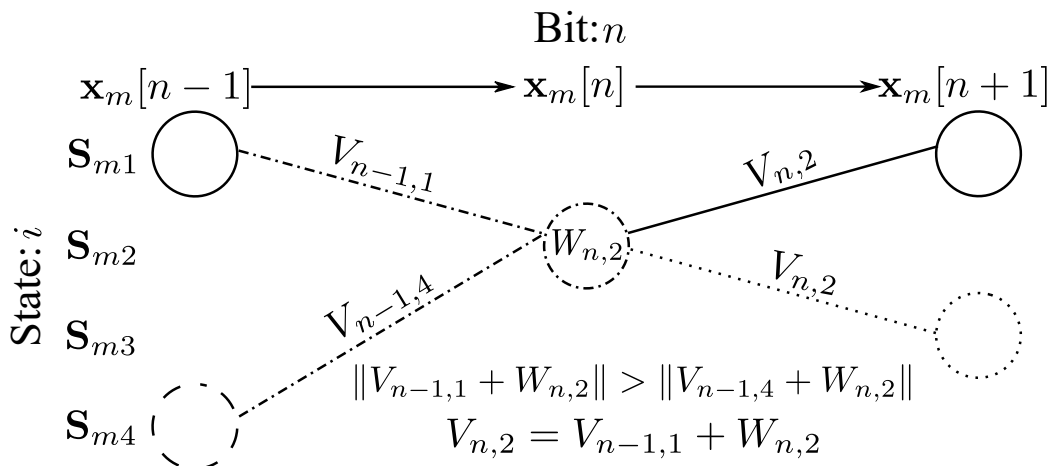


Figure 3.1: Toy example of the proposed algorithm, on a partial trellis diagram. $W_{n,i}$ refers to the complex weight of the n -th bit to be $\hat{\mathbf{x}}_m[n] = \hat{\mathbf{S}}_{mi}$. $V_{n,i}$ refers the complex cumulative weight of the surviving path that the n -th bit at the i -th state propagates forward. Note that the absolute values of the cumulative weights are compared, but instead, the complex value of the winning path is propagated to the next bit.

Again, Th. 1 enables the transition from the zero-centered to the β -centered signal model. The maximization problem of Eq. (3.7), if solved naively with exhaustive techniques among all valid N -bit Miller sequences, it entails exponential complexity (there are 2^N possible sequences). Prior art of [24] on GLRT optimal noncoherent detection (for coded sequences), provides substantial work that can be applied to Miller coded sequences. Using aforementioned methods, the GLRT optimal sequence can be detected with quadratic complexity (N^2).

However, even the quadratic complexity algorithm takes too long when $N = 128$ (in the case of Gen2), considering the strict time limits the Gen2 protocol imposes. Thus, a novel linear algorithm is offered below

It is crucial to understand that the proposed algorithm is *not* designed to solve the GLRT detection problem. Specifically, it tries to approximate the inner cumulative complex weight that maximizes the Euclidean norm of Eq. (3.7). This means that the proposed linear algorithm is suboptimal GLRT-wise. Surprisingly enough, not only does it provide low complexity (linear to the sequence length), but also near-optimal BER performance,

according to the numerical results, even compared to the ideal (perfect CFO, DC, CSI knowledge) coherent sequence detection.

3.2.1 Algorithm

Intuitively, one could think of this algorithm as a modification of the VA. A trellis diagram (Fig. 2.2) is utilized to take into account the allowed Miller transitions, but instead of using real valued weights for each trellis node, complex weights are used given by the inner product $W_{n,i} = \langle \hat{\mathbf{x}}_m[n], \mathbf{y}_m[n] \rangle$; n refers to the n -th bit, and i refers to the state of the trellis diagram, i.e., $\hat{\mathbf{x}}_m[n] = \hat{\mathbf{S}}_{mi}$. Since this algorithm uses complex weights, it is impossible to compare the metrics and choose a winning path (as done in the classic VA). The plot twist comes from the fact that the comparison happens between the absolute values of the complex weights. This means that for each node of the diagram the incoming cumulative weights (complex) are added to the node's inner product, in turn the absolute values of the sums are compared, and the largest (in terms of absolute value) complex cumulative weight is kept. The latter complex weight of the winning/surviving path is propagated to the next bit's nodes.

The above procedure is demonstrated in the toy example of Fig. 3.1. In this example, the node under examination is that of the n -th bit and \mathbf{S}_{m2} state, with inner product weight equal to $W_{n,i} = \langle \hat{\mathbf{S}}_{m2}, \mathbf{y}_m[n] \rangle$. This node has two incoming cumulative complex weights from states \mathbf{S}_{m1} and \mathbf{S}_{m4} , named $V_{n-1,1}$ and $V_{n-1,4}$, respectively. For the sake of the example, it is assumed that the winning path is the one coming from the state \mathbf{S}_{m1} , and thus, $\|V_{n-1,1} + W_{n,2}\| > \|V_{n-1,4} + W_{n,2}\|$. So, the outgoing weight of the examined node becomes: $V_{n,2} = V_{n-1,1} + W_{n,2}$. The last equality can be expanded, and with some freedom in terms of notation, it can be shown that:

$$\begin{aligned} V_{n,2} = V_{n-1,1} + W_{n,2} &= \left(\sum_{k=0}^{n-1} \langle \hat{\mathbf{x}}_m[k], \mathbf{y}_m[k] \rangle \right) + \langle \hat{\mathbf{x}}_m[n], \mathbf{y}_m[n] \rangle \\ &= \sum_{k=0}^n \langle \hat{\mathbf{x}}_m[k], \mathbf{y}_m[k] \rangle. \end{aligned} \quad (3.8)$$

Algorithm 1: Linear Noncoherent Miller 2/4/8 Sequence Detection

Input: m, \mathbf{y}_m
Output: X_{bits}

- 1 Initialize $p[4][N-1], w[4][N], v[4][N]$ to zeros
- 2 $w[1][1], v[1][1] = \langle \hat{\mathbf{S}}_{m1}, \mathbf{y}_m[1] \rangle$
- 3 $w[3][1], v[3][1] = \langle \hat{\mathbf{S}}_{m3}, \mathbf{y}_m[1] \rangle$
- 4 **for** $n = 2 : 1 : N$ **do**
- 5 **for** $i = 1 : 1 : 4$ **do**
- 6 $w[i][n] = \langle \hat{\mathbf{S}}_{mi}, \mathbf{y}_m[n] \rangle$
- 7 $j^* = \underset{j \in \mathbb{P}(n,i)}{\operatorname{argmax}} \|v[j][n-1] + w[i][n]\|_2$
- 8 $p[i][n-1] = j^*$
- 9 $v[i][n] = v[j^*][n-1] + w[i][n]$
- 10 $j^* = \underset{j \in \{1,2,3,4\}}{\operatorname{argmax}} \|v[j][N]\|_2$
- 11 $X_{\text{bits}}[N] = \mathbb{I}(j^* \leq 2)$
- 12 **for** $n = N-1 : -1 : 1$ **do**
- 13 $j^* = p[j^*][n]$
- 14 $X_{\text{bits}}[n] = \mathbb{I}(j^* \leq 2)$
- 15 **return** X_{bits}

Setting $n = N - 1$, and selecting:

$$V^* = \operatorname{argmax} \|V\|_2^2, V \in \{V_{N-1,i} \mid \forall i \in \{1, 2, 3, 4\}\}, \quad (3.9)$$

yields an approximation to the optimal complex weight that maximizes the absolute value of Eq. (3.7).

3.2.2 Algorithm Notation

The proposed algorithm in tabulated form is given above; as far as notation goes, $w[4][N]$ is an array that stores complex inner products for each node of the trellis diagram (equivalent to $W_{n,i}$); array $v[4][N]$ stores cumulative complex weights of each winning path (equivalent to $V_{n,i}$). The array $p[4][N-1]$ stores the winning path selection (in the case of the toy example

$p[2][n-1] = 1$). Finally, $\mathbb{P}(n, i) \subset \hat{\mathbb{S}}_m$ is a set that contains the symbols that allow the transition to the n -th bit and i -th state node, according to the Miller line coding. In the case of the toy example $\mathbb{P}(n, 2) = \{1, 4\}$.

Chapter 4

Multistatic RFID Reader Architecture

Schematic visualizations of the proposed system can be seen in Fig. 4.1 and Fig. 4.2. $M + 1$ Ethernet-enabled SDRs are utilized, where M are Tx SDRs and 1 is Rx. Note how all of them are connected on the same local area network (LAN). A host PC is also connected on the same LAN in order to control the operation of the SDRs and distribute the Gen2 interrogation process accordingly. By utilizing multiple Tx components, the chance that a tag is located near an illuminator, and thus activate, increases dramatically. As already discussed in prior art, but also in this work, multistatic architectures offer several advantages compared to their monostatic counterpart, however they are harder to implement.

Fig. 4.3 demonstrates how the interrogation is distributed to Tx and Rx SDRs through the Ethernet. The transmitting SDR is responsible for powering the Tag (CW), as well as transmitting QUERY and ACK messages; the receiving SDR has to capture the backscattered RN16 and EPC messages. Decoupling the Tx and Rx components of an RFID interrogator is a challenging procedure, which will be described in the following sections.

4.1 Software Implementation with SDRs over Ethernet

The signal processing chain is showcased in Fig. 4.4, in which baseband samples are generated and transmitted (Tx SDR) and received (Rx SDR) for processing in the host PC. All this procedure is operated by custom software developed in C++ for use alongside the GNURadio framework, and

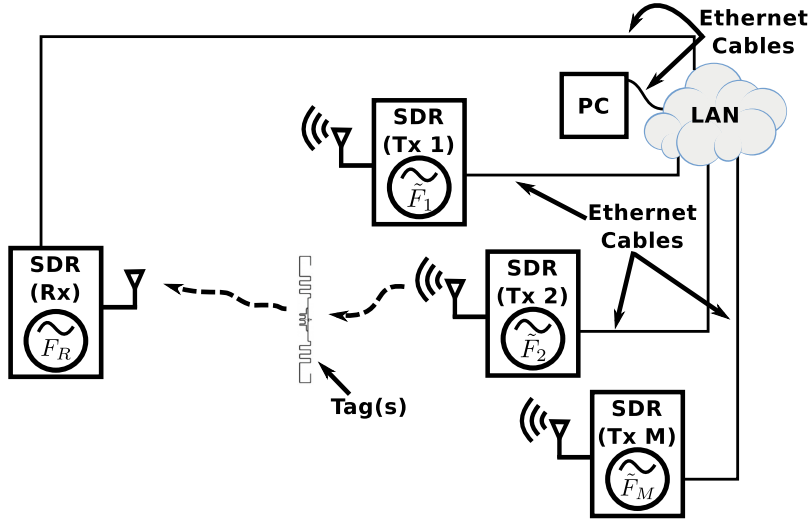


Figure 4.1: Proposed multistatic architecture for real-time, Ethernet-based RFID tag interrogation. Multiple inexpensive SDRs are employed.

it's based on prior work of [22, 25].

The tag interrogation process starts from the Tx SDR, by transmitting a continuous wave (CW) which activates the tags (through RF energy harvesting) located near the illuminator.¹ The host PC now generates baseband samples for QUERY command, and forwards them via Ethernet to one of the M available Tx SDRs which the Tx SDR transmits. In turn, the Rx SDR captures the interrogation and forwards (via Ethernet) baseband I/Q samples back to the host PC.

Now it's time for the host PC to process these samples so as to proceed with the interrogation. However, the first challenge that comes with multistatic setups is the carrier frequency offset between the Tx and Rx units, which deforms the received samples. As shown in Fig. 4.1, each SDR utilizes a different oscillator, and thus each SDR is tuned to a different frequency ($F_R, \tilde{F}_1, \tilde{F}_2, \dots, \tilde{F}_M$). In this work, the CFO is compensated using a phase locked loop (PLL), which will be discussed more thoroughly in Sec. 4.2. Having removed the CFO (as good as a PLL can), matched filtering is performed on the compensated samples, and then the host PC can actually start op-

¹Note that this CW is present throughout the interrogation process; the only exception to that is when the reader is transmitting a command, i.e., QUERY or ACK.

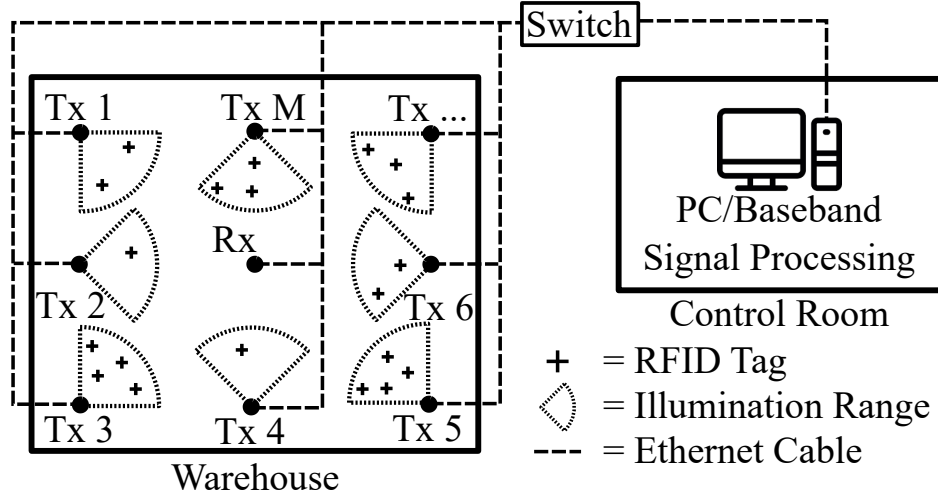


Figure 4.2: The vision of the proposed architecture. Multiple SDR transmitters/illuminators are deployed in a warehouse, and a single SDR receiver. Each illuminator activates a specific sector, due to the tag’s RF harvesting sensitivity. Assuming multiple transmitters, a large area can be covered. The system avoids lossy and expensive coaxial extension cables and amplifier units by using conventional SDRs networked through Ethernet.

erating on the output of the matched filter. The host PC needs to detect, and synchronize with the command transmitted from the Tx SDR (in this case it’s the QUERY). Between the QUERY and the RN16 (tag’s response), there is a time interval where the only signal “in the air” is the CW of the illuminator. This time interval is known, and thus by synchronizing with the QUERY, one can estimate the DC offset via a sample mean operation, and then remove it from subsequent samples, in order to isolate the tag’s response (RN16). With the CFO and DC offset out of the way, synchronization (via the known Gen2 preamble bits) and detection of the RN16 is possible. Detection can be performed with either coherent or noncoherent sequence detection. However, opting for coherent detection requires CSI estimation, which as shown later in this work, under-performs in terms of BER, due to the residual CFO. Having detected the RN16 bits, the host PC can generate the ACK samples and forward them to one of the M available Tx SDRs. The above procedure is repeated, for the reception and detection of the tag’s EPC bits.

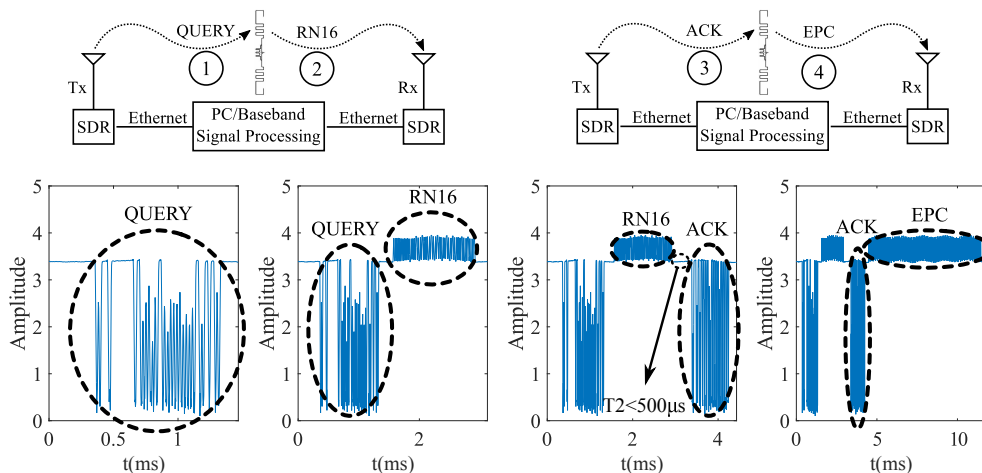


Figure 4.3: Distributed Gen2 RFID interrogation, captured from bistatic operation using 2 USRP N200 SDRs (one for Tx and one for Rx).

4.2 Real Time CFO Estimation/Housekeeping Tasks

As already mentioned, the most challenging problem of the proposed setup is the one of real-time CFO tracking and compensation. The Gen2 protocol defines a stringent time constraint between the end of the RN16 and the start of the ACK. Specifically, the protocol forces the reader to start transmitting the ACK command within $T2$ seconds from the last symbol of the RN16. According to the nominal values the protocol defines, it holds that: $\frac{3}{BLF} \leq T2 \leq \frac{20}{BLF}$, where BLF stands for backscatter link frequency (which is inversely proportional to the symbol duration). In this work BLF is set to the lowest possible value which is $BLF = 40 \text{ KHz}$. In other words, reader has to transmit the ACK within $T2 = 500 \mu s$, or the tag will timeout itself. The $T2$ time interval is shown in Fig. 4.3.

This time constraint, calls for a design of algorithms and solutions fast enough to be able to perform housekeeping (CFO & DC compensation, synchronization) and data detection (RN16) within $T2$ seconds. Although a high-resolution, periodogram-based solution (Fast Fourier Transform (FFT) on large sample blocks) for the CFO compensation would be optimal, it

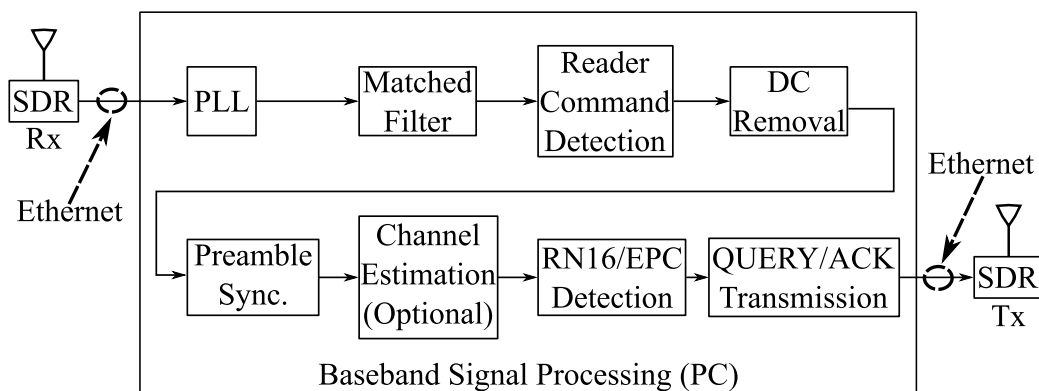


Figure 4.4: Block diagram that showcases the flow of the generated/received samples, through the various processing stages of the proposed system.

would take too much time for this application, and thus it is deemed unsuitable. Instead, a digital phase locked loop (PLL) was facilitated (see Fig. 4.5), because of its real-time character, low-complexity, and high reconfigurability.

The PLL in use for simulations and testing, was designed according to the resources offered in [26, App. C]. Namely, a second order loop filter was implemented, using both theory as well as trial-and-error (based on experimental waveforms), in order to fine tune the various PLL parameters. Concerning the simulations, the CFO tracking was active only during the time intervals where CW is present alone (no QUERY, ACK, RN16, EPC). After tracking the CFO and storing the detected phases (output of PLL), the CFO was estimated by solving a least squares-based [27], best linear fit problem (CFO is the slope of estimated line). This estimate is used to correct the subsequent important samples that include the RN16 or EPC.

As a means of determining how good the PLL works, the cumulative density function (CDF) of the absolute residual CFO is simulated (see Fig. 4.6). The simulation consisted of 10^5 Monte Carlo experiments where the initial CFO of the signal was randomly and independently selected from a uniform distribution, $\mathcal{U}(-10^5, +10^5)$ Hz. Note that in Fig. 4.6 a second CFO estimation method is offered that performs as good as the PLL. This method is based on the ML phase estimator, $\hat{\phi} = \arctan\left(\frac{\Im\{\cdot\}}{\Re\{\cdot\}}\right)$, coupled with a linear fit scheme to estimate the slope (i.e., Δf) of the line, as done with the PLL.

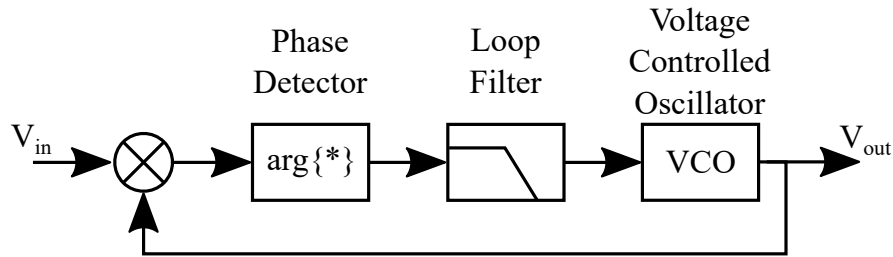


Figure 4.5: A simple schematic of a phase locked loop (PLL) used to track and compensate the CFO.

Even though, both methods perform equally in terms of residual CFO, the PLL is a better option, because of the real-time character (explained below), and its customizability.²

The PLL discussed above was integrated to the GNURadio library as an external block (coded in C++), for experimental benchmarking. The final system was functional, however, the *"PLL carrier tracking"* GNURadio block was used in its place, for the sole reason that it outperformed this works implementation.³ The built-in PLL is connected after the source (Rx SDR) and before the matched filter, as shown in Fig. 4.4, and it's operating throughout the whole interrogation process (not only during the CW), thus there is no need CFO estimation through a linear fit.

Figure 4.7 provides a graphical illustration of the received samples (Rx SDR), for the proposed multistatic setup (see Fig. 5.7), as well as the various processing steps they go through in order to detect the backscattered data.

There is no need to directly compensate the CPO, since it's a constant phase that gets absorbed by the channel parameter. In both cases of coherent and noncoherent detection, this does not affect any part of the system.

Synchronization on symbol level for RN16 and EPC is discussed in [22,23] for Gen2 FM0 and Miller cases, accordingly. In this work, it's performed in the same fashion, i.e., a correlation metric is maximized, exploiting the build-

²Selecting appropriate parameters for the PLL is crucial to achieve optimal performance, and in this work these parameters are far from that point. Meaning that the PLL could potentially outperform the heuristic method.

³Clearly, this works PLL design can be enhanced, but this is out of the scope of this thesis.

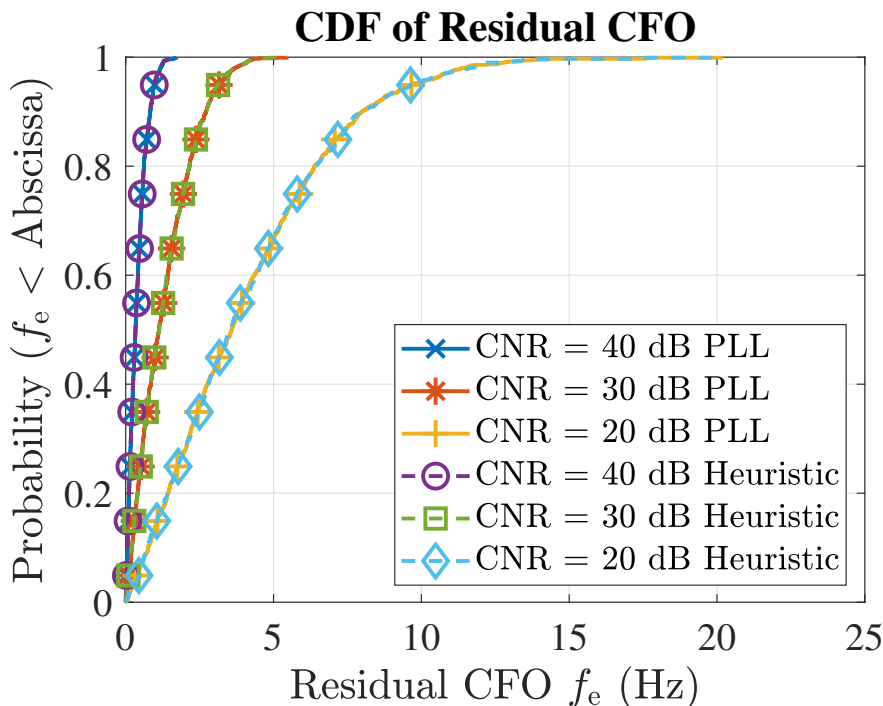


Figure 4.6: Simulated cumulative density function (CDF) of the absolute residual CFO after compensation using either a PLL or a heuristic method.

in 10-bit (Miller case) preamble sequence of Gen2. Alternatively, energy-based synchronization can be performed on a packet-wide (RN16 or EPC) window, so as to drop any dependencies from the preamble bits.

Estimation of the channel parameter is also described for Gen2 in the above references. Specifically, in this work, it is performed using a least squares technique on the 10-bit preamble sequence of Gen2, as shown in Eq. (3.6), utilizing the original β -centered symbols instead. It is noted that Gen2 offers the option to activate an additional 12-bit pilot sequence, at the expense of tag reading rate, but it's not activated in this work.

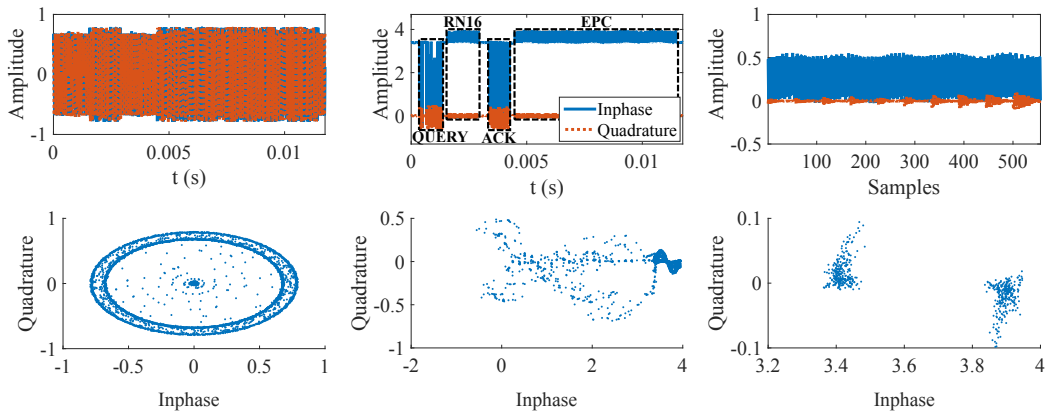


Figure 4.7: SDR-captured experimental waveforms (Top) & respective scatter plots (Bottom) of the received waveforms. Received waveform prior to CFO compensation (Left), after PLL-based CFO removal (Middle) and after DC compensation & synchronization (Right).

4.3 Limitations

In this work, every proposed algorithm and solution has very low complexity. Thus, given a sufficiently strong machine to operate the system,⁴ the signal processing can be performed in a timely manner. The limitation of this system is the Ethernet layer and the delays that occur from transferring data through different machines (host PC, Ethernet switch, multiple SDRs). Although Ethernet works for small tag rates (this work uses the lowest possible rate), it can quickly break the strict time limits that the Gen2 imposes, as the tag rate increases.

⁴A 7-year-old laptop was used in this work.

Chapter 5

Numerical Results

5.1 Simulation

As a means of verifying the functionality and robustness of the proposed architecture, a series of simulations were carried out based on the signal model of Eq. 2.1 and the detection algorithms studied in Chap. 3. The first set of simulations focused on a monostatic setup where CFO and DC are compensated perfectly. In the second set, CFO and DC compensation are considered imperfect, thus there is a small residue. In both scenarios, the bit error rate (BER) was examined for both detection schemes (coherent & noncoherent), under Rayleigh and Rician fading. In the case of Rician fading; $k_{CT} = k_{CR} = 20$ and $k_{TR} = 15$ for the bistatic setup and $k_r = k_{CT} = 20$ for the monostatic. SNR is defined as follows:

$$\text{SNR} = \frac{2P_c L s^2 \mathbb{E}[|\mathbf{x}_{\text{tag}}|^2] \sigma_{CT}^2 \sigma_{TR}^2}{\sigma_n^2}. \quad (5.1)$$

The following assumptions were made, without loss of generality; $P_c = 0.5$ W, $\sigma_{CT}^2 = \sigma_{TR}^2 = 1$, and $\mathbf{x}_{\text{tag}}[n] \in \{0, 1\}$. For each $\text{SNR} \in \{0, 1, \dots, 8\}$, 10^5 Monte Carlo experiments were carried out. Furthermore, according to Eq. (1.1), it is assumed that $m_{dc} = h_{CR}|\lambda_c|$, where $\lambda_c \in \mathbb{C}$ is a constant parameter that is connected to the Tx power and tag characteristics. Thus, the carrier to noise ratio (CNR, i.e., SNR of the direct link) can be defined as follows:

$$\text{CNR} = \frac{\mathbb{E}[|m_{dc}|^2]}{\sigma_n^2} = \frac{|\lambda_c|^2 \sigma_{CR}^2}{\sigma_n^2}. \quad (5.2)$$

Thus, for $\sigma_{CR}^2 = 1$, $m_{dc} = h_{CR}\sqrt{\text{CNR} \cdot \sigma_n^2}$. A direct link of $\text{CNR} = 30$ dB

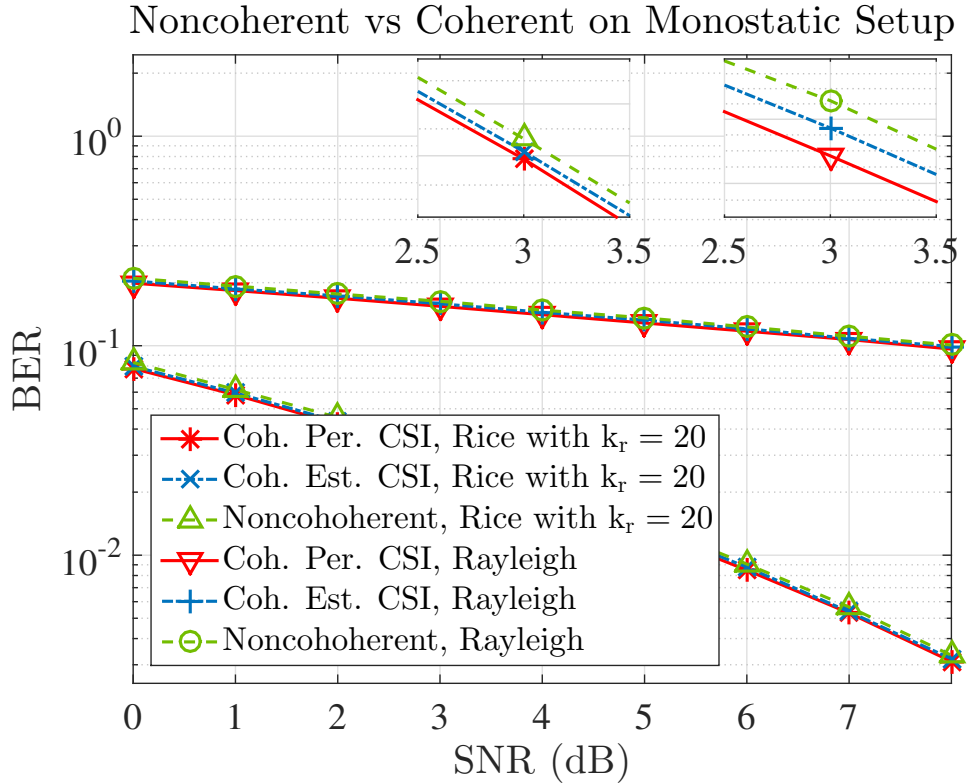


Figure 5.1: BER performance of the monostatic model with perfect CFO and DC compensation. The length of the sequence is $N = 128$ bits.

is assumed throughout the simulations, and sequence length of $N = 128$ bits was considered.

In the case of the monostatic setup (with perfect CFO and DC compensation) the BER performance of the proposed algorithms is examined in Fig. 5.1. Under Rician fading, the noncoherent scheme, performs about 0.2 dB worse than the perfect coherent scheme, while the coherent with estimated CSI performs about 0.05 dB worse than its perfect counterpart. Under Rayleigh fading, the aforementioned gaps increase to 0.5 dB and 0.25, dB respectively. Thus far, the proposed noncoherent algorithm seems to perform almost on par with the optimal coherent scheme of prior art.

Next, the bistatic model is examined, in Fig. 5.2, using the signal model of Eq. (1.1), $L = 125$, and real-world CFO tracking and removal as well as DC offset compensation. The former is performed using a PLL, while

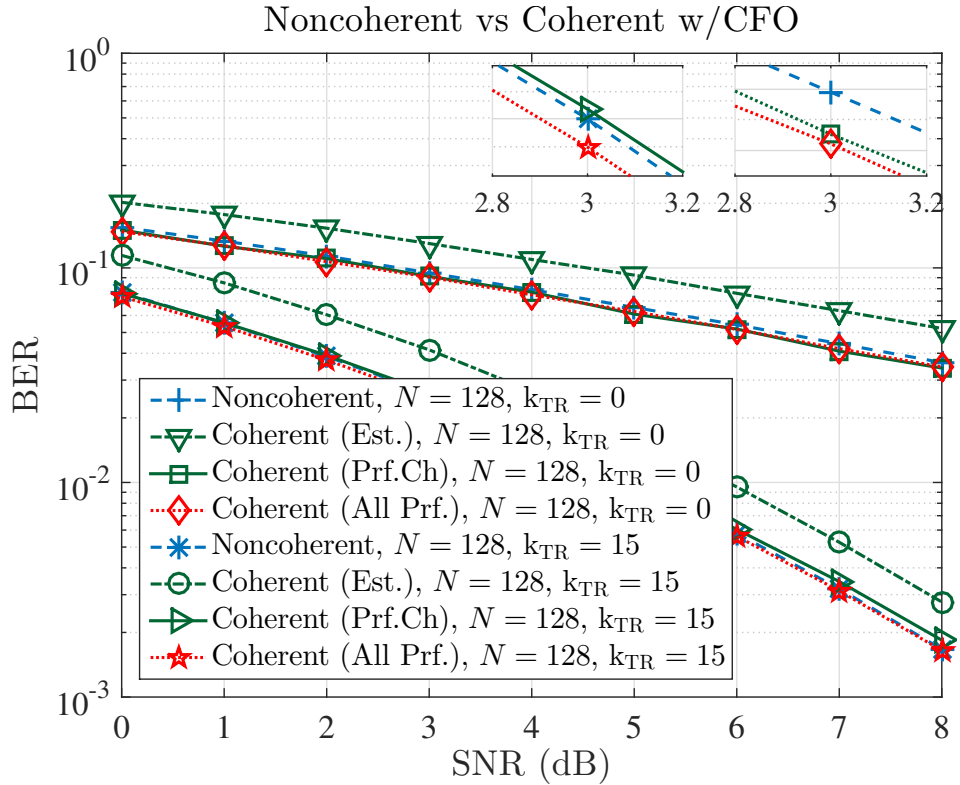


Figure 5.2: BER of the bistatic model with imperfect CFO compensation (using PLL) and dc offset correction. Performance gaps is demonstrated between coherent (with either perfect (Prf.Ch) or estimated channel (Est.)) and noncoherent detection, under Rayleigh and Rician fading conditions ($k_{CR} = k_{CT} = 20$). The case of perfect CFO and DC compensation is also given, as a baseline (All Prf.).

the latter is done by estimating the DC term through a sample mean over a specific time interval (where the only signal “in the air” is the CW, e.g., between QUERY and RN16), and then subtracting it from all the subsequent samples. As far as coherent detection is concerned, channel estimation was performed with a least squares method on the known preamble sequence that precedes every backscattered packet (RN16/EPC). By examining the results shown in Fig. 5.2, the first thing that draws the attention is that the coherent scheme with estimated channel (i.e., Coherent (Est.)) suffers from a severe performance degradation, even compared to the noncoherent detection. Specifically, the gap between Perfect coherent and estimated coherent

is about 1.5 dB and 1.2 dB, for Rayleigh and Rician fading, respectively.

This observation can be explained by the fact that, due to the remaining CFO, after the PLL, the flat fading assumption no longer holds, and as a result, channel estimation will be erroneous and will deteriorate the performance of the detection, especially as the sequence length increases. The previous statements are further highlighted by the fact that when the channel parameter is perfectly known, the BER gap between Coherent Prf. Ch. and Coherent All Prf. is reduced down to about 0.1 dB, for both Rayleigh and Rician fading. Another surprising observation is that in the case of Rician fading, the proposed noncoherent algorithm slightly outperforms the coherent algorithm with perfect CSI but imperfect CFO and DC compensation. This unintuitive observation can be understood as a result of the residual CFO interfering with the deterministic part of the Rician channel (non-zero mean value), resulting in altered statistics. In the case of Rayleigh channel, the mean value is zero, i.e., no deterministic component, thus, there is little impact on the statistics of the channel. As a result, both channel estimation and coherent detection can be performed more reliably under Rayleigh fading.

These simulations provide substantial proof that the linear complexity noncoherent Miller sequence detection algorithm, proposed by this work, is a robust and low complexity approach, that is advantageous over prior coherent schemes, that under-perform in the presence of CFO and weak channel estimation. The latter is a common problem in multistatic architectures. This also shows how later versions of Gen2 could drop training bits altogether in favour of increasing tag reading rate, without sacrificing robustness and computational power.

5.2 Experimentation

The experimental results are divided into two categories, those extracted from monostatic setups, and those from multistatic setups.

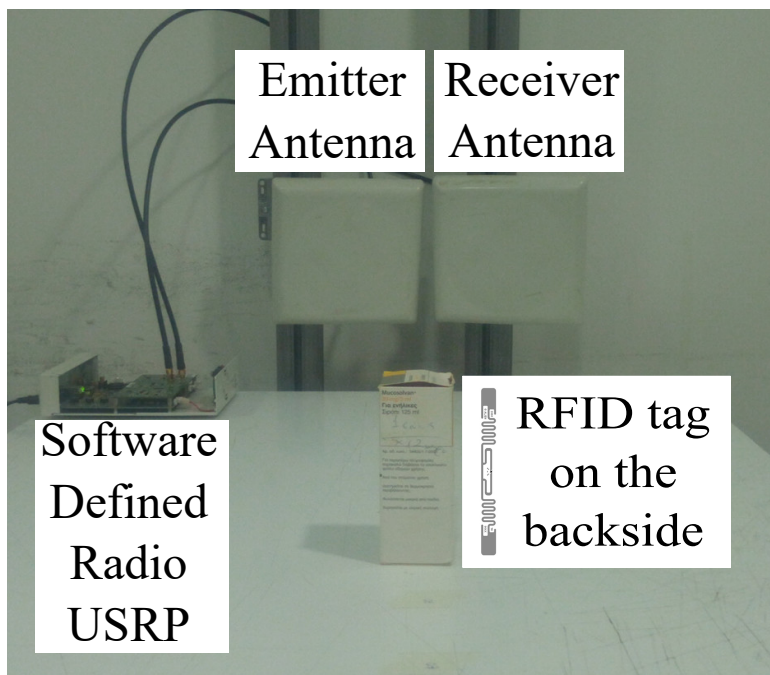


Figure 5.3: Monostatic setup used to extract experimental results for the proposed noncoherent detection algorithm.

5.2.1 Monostatic Setup

Fig. 5.3 shows the experimental testbed used to extract measurements in a monostatic setup. The apparatus consists a USRP N200 SDR (used for both Tx and Rx) which is wired to a commodity laptop via Ethernet. An RFX900 daughterboard is mounted on top of the SDR; two MTI MT-242032 7 dBi antennas (one for Tx, one for Rx) are connected to the daughterboard via 0.74 dB loss coaxial cables. The industrial Gen2 RFID used in this setup is the Alien ALN-9540 (Higgs-2). Finally, the daughterboard was tuned to operate at 865 MHz with 13 dBm Tx power.

The software stack is based on prior work found in [22], and it was augmented to support Miller 2 line codes. Specifically, the software is capable of decoding Miller 2 waveforms using: bit-by-bit coherent detection, coherent sequence detection, and the proposed noncoherent sequence detection algorithm. 10^4 interrogations were carried out for each algorithm and each distance setup. The captured waveforms were stored in order to be rerun

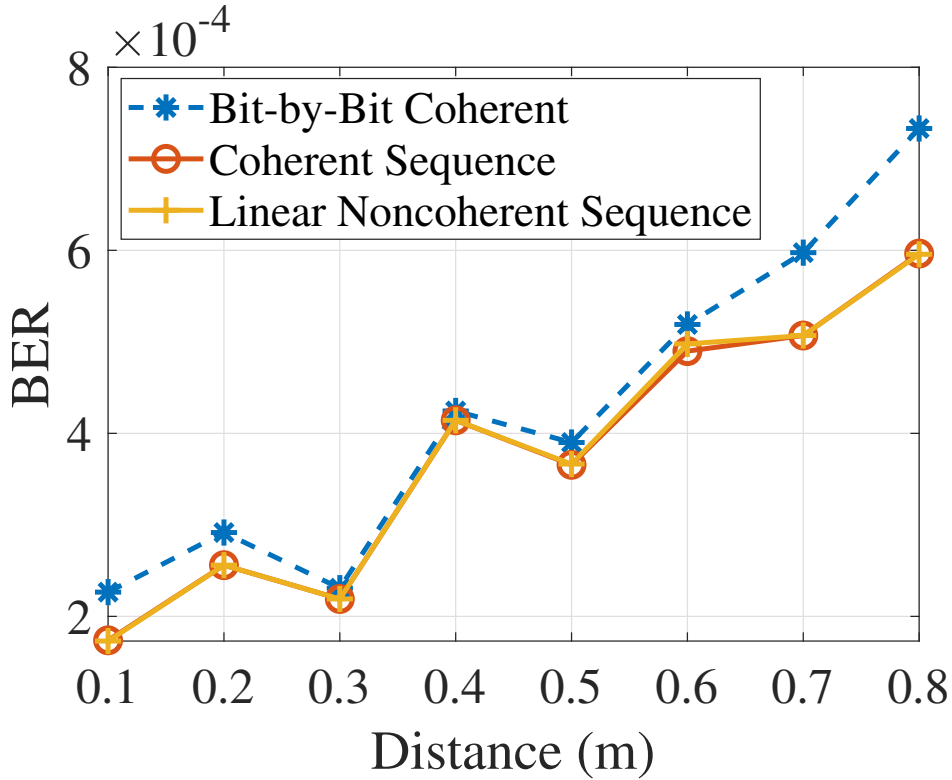


Figure 5.4: Comparison of experimental BERs extracted on a monostatic RFID setup, using various detection algorithms.

“offline” using the rest detection algorithms. This cross-testing provided a fair comparison for the BER performance of the discussed algorithms.

Thus, experimental BERs were extracted for the monostatic setup. It needs to be noted that some waveforms were discarded; this was done when about half of detected bits were wrong. Specifically, a threshold of 35% was used to determine whether a packet is lost or not. These cases can be explained by a lack of tag response or bad synchronization, and not by fault of the detection algorithms.

Fig. 5.4 demonstrates how the proposed noncoherent sequence detection and the coherent sequence detection algorithm performs equally in terms BER. As discussed in prior art, bit-by-bit coherent detection of Miller sequences under-performs compared to its sequence-based counterpart.

Considering the high SNR, resulted by strong line of sight, and small

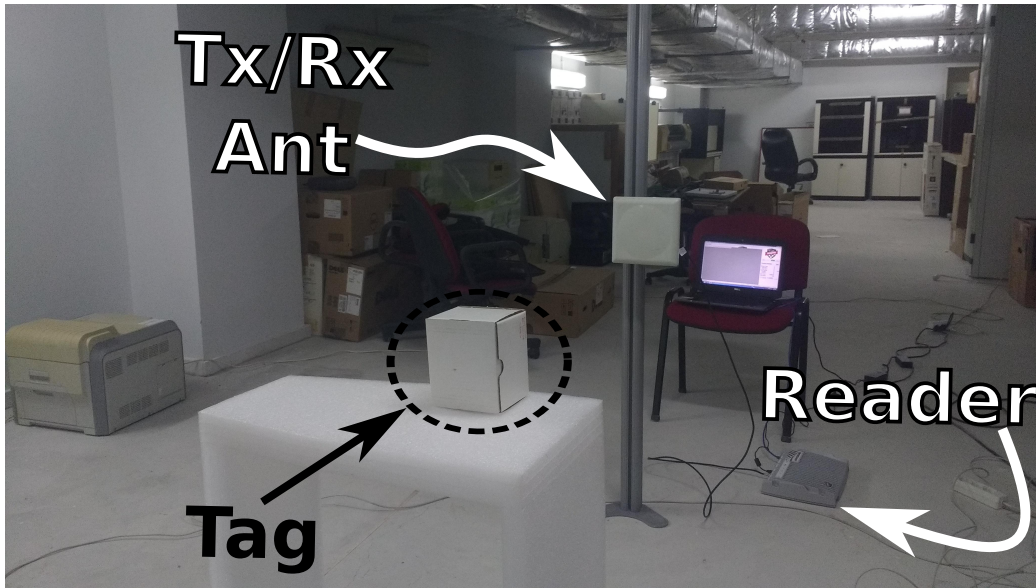


Figure 5.5: Monostatic setup with commercial RFID reader under harsh indoor conditions. This offered a baseline for the tag reading distance. With 15 dBm Tx power, a maximum communication range of 1.1 m was achieved, while for 30 dBm the range increased to 4.5 m.

distances (due to tag’s poor RF harvesting sensitivity), the aforementioned experimental figure validates the simulated results for the monostatic case.

5.2.2 Multistatic Setup

Before diving into testing the multistatic setup, a monostatic setup based on the Impinj Speedway R1000 RFID reader was used in order to extract a baseline reference for the following measurements under harsh indoor conditions (see Fig. 5.5). An MTI MT-242032 7 dBi antenna was wired to the reader via a 0.74 dB loss coaxial cable. The tag used in this experiment was an Alien ALN-9741 (Higgs-4) industrial Gen2 RFID tag. Using the reader’s software, configurations were made so as to interrogate the tag at the 865 – 868 MHz band, as well as to operate at either 15 dBm or 30 dBm (Tx power at the cable of the antenna). Note that the reader’s Tx power and the cable loss were measured by a spectrum analyzer and a VNA, respectively. The antenna was placed at about 0.9 m from the ground, and the testing facility was full of

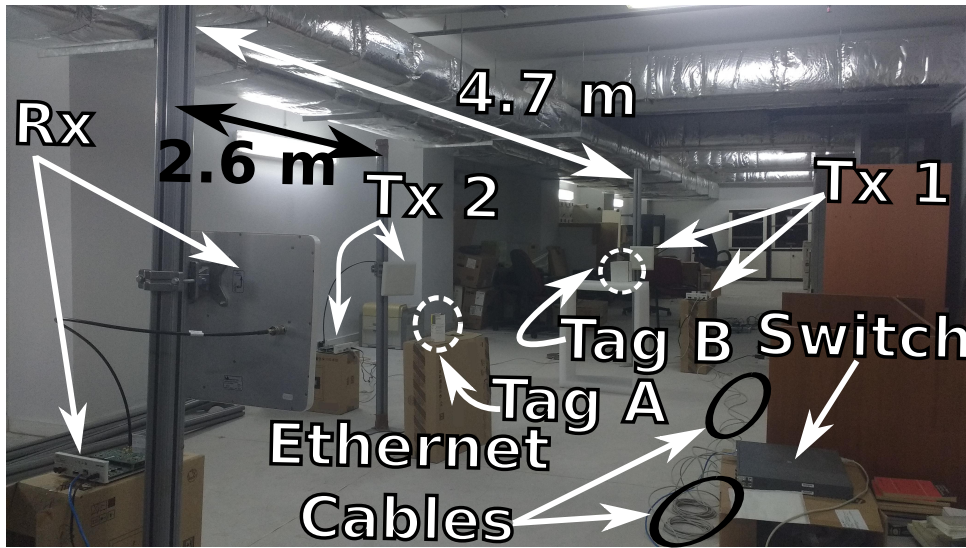


Figure 5.6: The proposed multistatic setup facilitating two USRPs as carrier sources/illuminators operating at 15 dBm alongside an RTL-SDR (or a USRP) as a receiver. The architecture offers increased coverage with multiple distributed SDR illuminators that function in a time-division manner and networked over Ethernet.

reflective materials, thus creating a rich scattering environment (Fig. 5.5). In the case of 15 dBm Tx power, the reader was able to interrogate the tag from a distance of 1.1 m. When the Tx power increased to 30 dBm, the distance also scaled up to 4.5 m.

The above experiment was done so as to define the interrogation sector, inside which an RFID tag can harvest enough energy to activate and backscatter its message. If the tag is outside this sector, it won't activate, thus, by distributing multiple illuminators in an area of interest, increased coverage can be achieved.

The first multistatic setup is demonstrated in Fig. 5.6. It is based on multiple Ettus N200 USRPs alongside FLEX900 daughtercards, which are connected via Cat5e Ethernet cables to an HP Procurve 2824 Ethernet switch. Specifically, this setup utilizes $M = 2$ transmitting SDRs (tuned at 865 MHz, with 15 dBm Tx power), wired to the aforementioned 7 dBi antennas, via 0.4 dB loss coaxial cables. On the receiving end, the Rx SDR used was also an N200, connected to an MT-242017, 10 dBi antenna. The developed software,

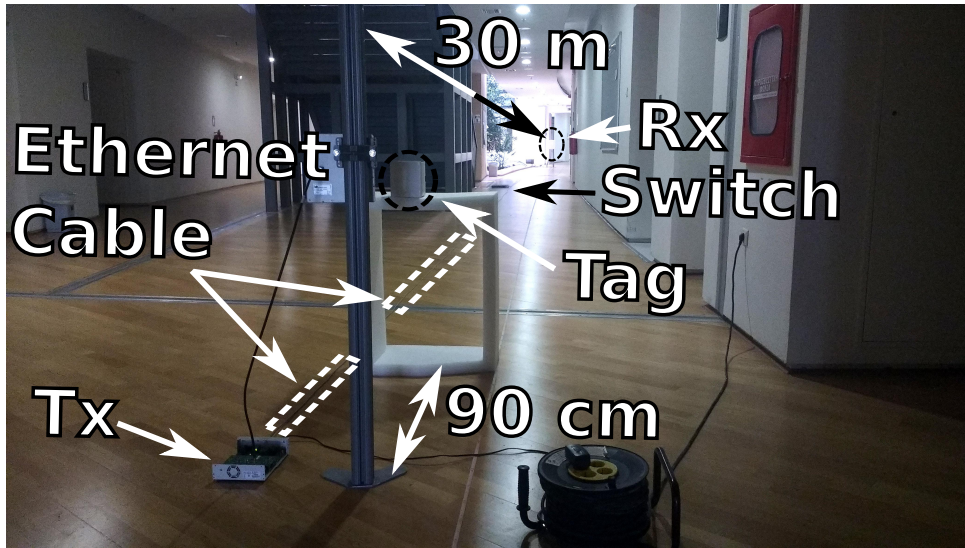


Figure 5.7: Demonstration of how a bistatic setup utilizing a single USRP as Tx (15 dBm) and a USRP or RTL-SDR as Rx, can increase reading range. Carrier-to-receiver ranges of at least 30 meters were observed, for a carrier-to-tag distance of 90 cm.

responsible for operating this multistatic setup, was running on a commodity laptop, which was also wired onto the Ethernet switch. Concerning the various distances in the setup of Fig. 5.6, the Tx-1 antenna was placed 4.7 m away from the Rx antenna, while the Tx-2 antenna was placed 2.6 m away. The aforementioned tags, Tag A = ALN-9540 and Tag B = ALN-9741, were placed inside the illuminating sector of Tx-2 and Tx-1 antenna, respectively. Specifically, Tag A was 0.7 m away from Tx-2, and Tag B was 1.1 m away from Tx-1. The software operated the two transmitting SDRs in a round-robin fashion (any scheduling is possible), and both tags were successfully interrogated. However, note that when Tx-1 was active, then only Tag B was interrogated, and vice versa for Tx-2 and Tag A. Thus, this test demonstrates in a realistic environment how multiple transmitters can increase coverage, due to higher probability of a tag being in the vicinity of an illuminator.

In addition to that, further feasibility of inexpensive and modular implementation is shown by swapping (on the Rx part) the Ettus N200 USRP with a \$7 RTL-SDR dongle, connected via USB 2.0 to the host laptop. This

Carrier-Tag Distance	Tag Reading Rate	
	N200	RTL-SDR
$d_{CT} = 40$ cm	161/268	27/600
$d_{CT} = 50$ cm	132/300	16/1000
$d_{CT} = 60$ cm	133/600	24/1000
$d_{CT} = 70$ cm	64/170	3/1000
$d_{CT} = 80$ cm	124/359	18/1000
$d_{CT} = 90$ cm	81/160	23/1000
$d_{CT} = 1$ m	572/1000	10/1000
$d_{CT} = 1.1$ cm	20/50	—

Table 5.1: This table offers tag reading rates, for either USRP N200 or RTL-SDR as the Rx SDR of the setup. Carrier-to-Receiver distance was set to 4.7 m, whereas Carrier-to-Tag distance (d_{CT}) was flexible to examine the behavior of the setup. A successful read/interrogation is equivalent to detecting all of the EPC bits of the tag correctly.

inexpensive dongle was capable of interrogating both tags, but there was a substantial reduction in the tag reading rate, mostly due to large buffer size of the RTL, alongside with the low bit-rate of USB 2.0 (whereas USRP N200 boasts a 1Gbit Ethernet connection).

On the same multistatic setup, facilitating either N200 or RTL-SDR for reception, tag reading rates (from a single iteration of the algorithm) were extracted and shown in Table 5.1, for various Carrier-to-Tag distances. It can be roughly observed that, as the Carrier-to-Tag distance increases, the tag reading rate fluctuates in a decreasing fashion, which can be explained by the indoor wireless propagation, and how the reflected signals in this rich scattering environment add up constructively or destructively.

The final experimental setup (see Fig. 5.7) seeks to showcase how the Tx-to-Tag link is the limiting factor in the reading range of passive tags. By using a bistatic setup with Tx-to-Rx distance equal to 30 m, and Tx-to-Tag (ALN-9741) equal to 0.9 m, the reader was able to successfully interrogate the tag using both N200 and RTL-SDR (on the Rx part).

Chapter 6

Conclusion

6.1 Conclusion

The proposed linear noncoherent algorithm has demonstrated high performance, even compared to ideal coherent detection, both in monostatic and multistatic setups, in simulations and realistic experimental testbeds. This highlights its suitability for use in harsh, time-constraint scenarios, where CFO and DC offset interfere with the integrity of the signal. Furthermore, the proposed multistatic architecture has managed to interrogate a tag 30 m away from the Rx antenna, as well as being capable of using multiple illuminators to increase coverage. Surprisingly, the noncoherent algorithm outperforms the coherent algorithm in a realistic multistatic setup, which further amplifies the need to use robust noncoherent schemes for multistatic architectures.

6.2 Future Work

The future plan is to get rid of the Ethernet cables, and substitute them with wireless links, e.g., WiFi. Ideally, the contribution of this work will provide a substantial motive and framework for the convergence of contemporary (e.g., LAN) or future (e.g., cellular) network infrastructure with the RFID industry (Fig. 6.1).

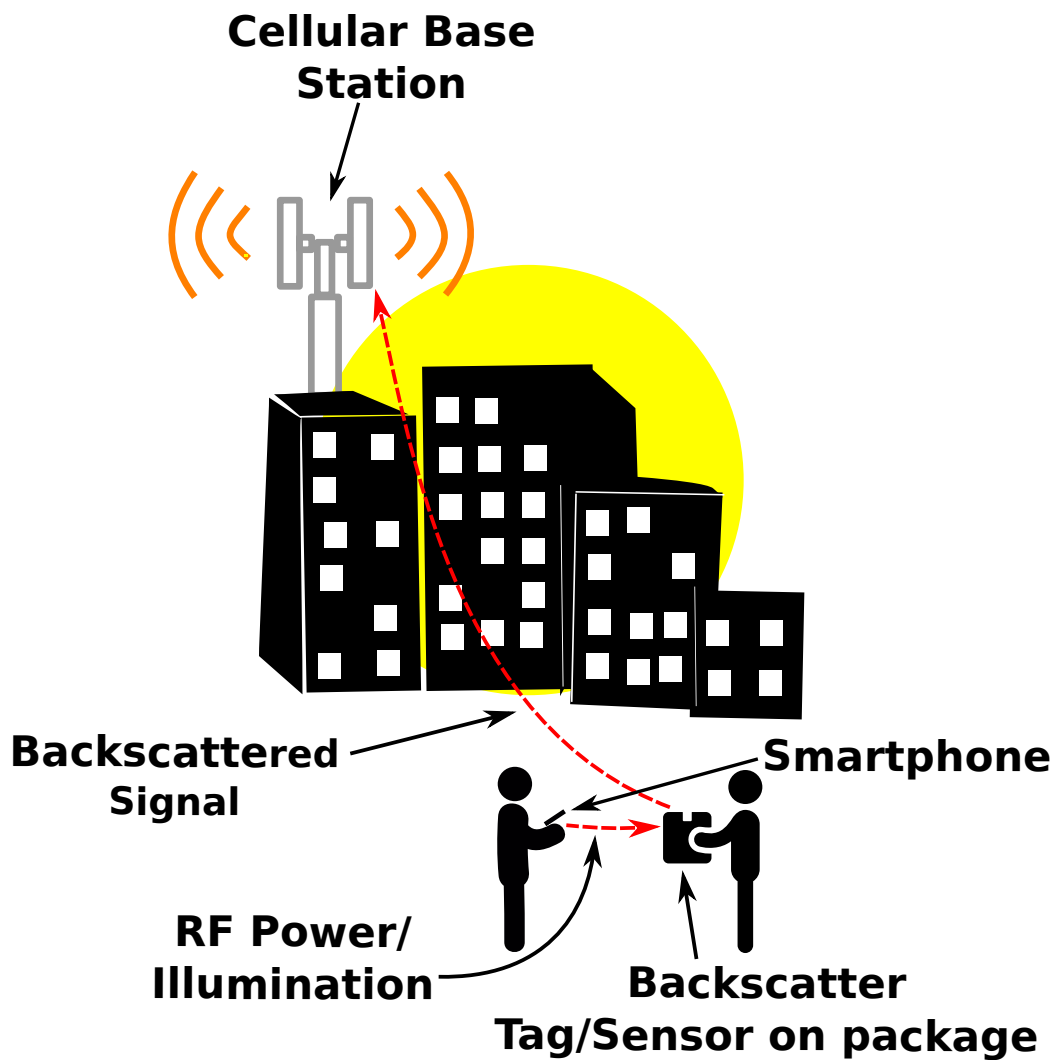


Figure 6.1: Would it be possible for contemporary (e.g., LAN) or future (e.g., cellular) network infrastructure to interrogate commercial Gen2 RFID or other IoT tags?

Bibliography

- [1] *EPC Radio-Frequency Identity Protocols, Class-1 Generation-2 UHF RFID Protocol for Communications at 860 MHz-960 MHz*. EPC Global, 2015, version 2.0.1.
- [2] M. Simon and D. Divsalar, “Some interesting observations for certain line codes with application to RFID,” *IEEE Trans. Commun.*, vol. 54, no. 4, pp. 583–586, April 2006.
- [3] R. Raheli, A. Polydoros, and C.-K. Tzou, “Per-Survivor Processing: A General Approach to MLSE in Uncertain Environments,” *IEEE Trans. Commun.*, vol. 43, pp. 354 – 364, Feb./Mar./Apr. 1995.
- [4] A. Polydoros and K. M. Chugg, “Per-Survivor Processing (PSP),” in *Wireless Communications: TDMA versus CDMA*. Boston, MA, USA: Springer, 1997, pp. 41–72.
- [5] P. N. Alevizos, Y. Fountzoulas, G. N. Karystinos, and A. Bletsas, “Log-linear-complexity GLRT-optimal noncoherent sequence detection for orthogonal and RFID-oriented modulations,” *IEEE Trans. Commun.*, vol. 64, no. 4, pp. 1600–1612, Apr. 2016.
- [6] M. Ouroutzoglou, A. Bletsas, and G. N. Karystinos, “Intelligent non-coherent sequence equals coherent detection: Experimental proof in industrial RFID,” in *7th International Conference on Modern Circuits and Systems Technologies (MOCASST)*, May 2018, pp. 1–4.
- [7] Y. Fountzoulas, D. Chachlakis, G. N. Karystinos, and A. Bletsas, “GLRT-optimal blind MSK detection with log-linear complexity,” in *2016 23rd International Conference on Telecommunications (ICT)*, May 2016, pp. 1–5.

-
- [8] I. Motedayen-Aval and A. Anastasopoulos, “Polynomial-complexity noncoherent symbol-by-symbol detection with application to adaptive iterative decoding of turbo-like codes,” *IEEE Transactions on Communications*, vol. 51, no. 2, pp. 197–207, Feb 2003.
- [9] J. Kimionis, A. Bletsas, and J. N. Sahalos, “Design and implementation of RFID systems with software defined radio,” in *Proc. IEEE European Conf. on Antennas and Propagation (EuCAP)*, Prague, Czech Republic, Mar. 2012, pp. 3464–3468.
- [10] —, “Bistatic backscatter radio for tag read-range extension,” in *Proc. IEEE RFID Techn. and Applications (RFID-TA)*, Nice, France, Nov. 2012.
- [11] —, “Bistatic backscatter radio for power-limited sensor networks,” in *Proc. IEEE Global Commun. Conf. (Globecom)*, Atlanta, GA, Dec. 2013, pp. 353–358.
- [12] —, “Increased range bistatic scatter radio,” *IEEE Trans. Commun.*, vol. 62, no. 3, pp. 1091–1104, Mar. 2014.
- [13] V. Liu, A. Parks, V. Talla, S. Gollakota, D. Wetherall, and J. R. Smith, “Ambient backscatter: Wireless communication out of thin air,” in *Proc. ACM SIGCOMM*, Hong Kong, China, Aug. 2013, pp. 39–50.
- [14] J. F. Ensworth and M. S. Reynolds, “Every smart phone is a backscatter reader: Modulated backscatter compatibility with bluetooth 4.0 low energy (BLE) devices,” in *Proc. IEEE RFID*, San Diego, CA, Apr. 2015, pp. 78–85.
- [15] P. N. Alevizos, K. Tountas, and A. Bletsas, “Multistatic scatter radio sensor networks for extended coverage,” *IEEE Trans. Wireless Commun.*, vol. 17, no. 7, pp. 4522–4535, Jul. 2018.
- [16] J. D. Griffin and G. D. Durgin, “Gains for RF tags using multiple antennas,” *IEEE Trans. Antennas Propag.*, vol. 56, no. 2, pp. 563–570, Feb. 2008.

-
- [17] R. Sadr *et al.*, “RFID systems using distributed exciter network,” Mar. 2013, US Patent 8,395,482 B2. [Online]. Available: <https://patents.google.com/patent/US8395482B2/en?q=US8395482>
- [18] Z. Fu, M. J. Crisp, S. Yang, R. V. Penty, and I. H. White, “Long distance passive UHF RFID system over ethernet cable,” in *Proc. IEEE RFID Techn. and Applications (RFID-TA)*, Warsaw, Poland, Sep. 2017, pp. 294–298.
- [19] V. Iyer, V. Talla, B. Kellogg, S. Gollakota, and J. Smith, “Inter-technology backscatter: Towards internet connectivity for implanted devices,” in *Proc. ACM SIGCOMM*, Florianopolis, Brazil, 2016, pp. 356–369.
- [20] V. Talla, M. Hesar, B. Kellogg, A. Najafi, J. R. Smith, and S. Gollakota, “Lora backscatter: Enabling the vision of ubiquitous connectivity,” *Proc. ACM Interact. Mob. Wearable Ubiquitous Technol.*, vol. 1, no. 3, pp. 105:1–105:24, Sep. 2017. [Online]. Available: <http://doi.acm.org/10.1145/3130970>
- [21] J. F. Ensworth and M. S. Reynolds, “BLE-Backscatter: Ultralow-Power IoT Nodes Compatible With Bluetooth 4.0 Low Energy (BLE) Smartphones and Tablets,” *IEEE Transactions on Microwave Theory and Techniques*, vol. 65, no. 9, pp. 3360–3368, Sep. 2017.
- [22] N. Kargas, F. Mavromatis, and A. Bletsas, “Fully-coherent reader with commodity SDR for Gen2 FM0 and computational RFID,” *IEEE Wireless Commun. Lett.*, vol. 4, no. 6, pp. 617–620, Dec. 2015.
- [23] E. Stratigi, “Synchronization, channel estimation and detection of RFID signals with Miller coding,” Diploma thesis available in: <http://dias.library.tuc.gr/view/72071>, School of ECE, Technical University of Crete, Chania, Greece, Feb. 2018, Supervisor A. Bletsas.
- [24] D. Chachlakis, “Optimal noncoherent trellis decoding,” Diploma thesis available in: <https://dias.library.tuc.gr/view/66126>, School of ECE,

-
- Technical University of Crete, Chania, Greece, Jul. 2016, Supervisor G. N. Karystinos.
- [25] M. Buettner and D. Wetherall, “A software radio-based UHF RFID reader for PHY/MAC experimentation,” in *Proc. IEEE RFID*, Apr. 2011, pp. 134–141.
- [26] M. Rice, *Digital Communications: A Discrete-time Approach*. Pearson/Prentice Hall, 2009.
- [27] S. M. Kay, *Fundamentals of statistical signal processing. [Volume I]. , Estimation theory*. Upper Saddle River (N.J.): Prentice Hall, 1993.